A high-resolution mapped grid algorithm for compressible multiphase flow problems

K.-M. Shyue

Department of Mathematics, National Taiwan University, Taipei 106, Taiwan

Abstract

We describe a simple mapped grid approach for the efficient numerical simulation of compressible multiphase flow in general multi-dimensional geometries. The algorithm uses a curvilinear coordinate formulation of the equations that is derived for the Euler equations with the stiffened gas equation of state to ensure the correct fluid mixing when approximating the equations numerically with material interfaces. A γ-based and a α-based model have been described that is an easy extension of the Cartesian coordinates counterpart devised previously by the author (K.-M. Shyue, An efficient shock-capturing algorithm for compressible multicomponent problems, J. Comput. Phys. 142 (1998) 208-242). A standard high-resolution mapped grid method in wave-propagation form is employed to solve the proposed multiphase models, giving the natural generalization of the previous one from single-phase to multiphase flow problems. We validate our algorithm by performing numerical tests in two and three dimensions that show second order accurate results for smooth flow problems and also free of spurious oscillations in the pressure for problems with interfaces. This includes also some tests where our quadrilateral-grid results in two dimensions are in direct comparisons with those obtained using a wave-propagation based Cartesian grid embedded boundary method.

Key words: Compressible multiphase flow, Fluid mixture model, Mapped grids, Wave propagation method, Stiffened gas equation of state
2000 MSC: 65M06, 65M50, 65Y15, 35L60, 58J45

Email address: shyue@math.ntu.edu.tw (K.-M. Shyue)

1. Introduction

Our goal is to describe a simple mapped grid approach for efficient numerical resolution of compressible multiphase flow in general multi-dimensional geometries. As a first endeavor towards the method development, we are concerned with a simplified model problem, where the flow regime of interest is assumed to be homogeneous with no jumps in the pressure and velocity (the normal component of it) across the material interface separating two regions of different fluid components within a spatial domain. In this problem, the physical effects such as the viscosity, surface tension, and heat conduction are assumed to be small, and hence can be ignored. With that, we use an Eulerian viewpoint of the governing equations that the principal motion of each fluid component in a Cartesian coordinates can be written as

$$\frac{\partial}{\partial t}\begin{pmatrix}\rho\\ \rho u_i\\ E\end{pmatrix}+\sum_{j=1}^{N_d}\frac{\partial}{\partial x_j}\begin{pmatrix}\rho u_j\\ \rho u_i u_j+p\delta_{ij}\\ E u_j+p u_j\end{pmatrix}=0 \tag{1}$$

for $i = 1, 2, \ldots, N_d$. Here N_d denotes the number of spatial dimensions. The quantities ρ, u_j, p, E, and δ_{ij} are the density, particle velocity in the x_j-direction, pressure, total energy, and the Kronecker delta, respectively.

To close the model, for simplicity, the constitutive law for each fluid phase is assumed to satisfy a linearized Mie-Grüneisen (*i.e.*, the linearly density-dependent stiffened gas) equation of state of the form

$$p(\rho, e) = (\gamma - 1)\,\rho e + (\rho - \rho_0)\,\mathcal{B} \tag{2}$$

for approximating materials including compressible liquids and solids (cf. [14, 25]). Here e represents the specific internal energy. The quantities γ, ρ_0, and $\mathcal{B}$ are the ratio of specific heats ($\gamma > 1$), the reference values of density, and speed of sound squared, respectively. We have $E = \rho e + \sum_{j=1}^{N_d} \rho u_j^2/2$ as usual.

In this work, we want to generalize a state-of-the-art shock-capturing method that was devised originally for single-phase flows on mapped grids to the case of a multiphase flow. It is well known that the principal problem in the usual extension is the occurrence of spurious pressure oscillations when two or more fluid components are present in a grid cell (cf. [5] and references therein). Here the algorithm uses a curvilinear coordinate formulation of a fluid-mixture model that is composed of the Euler equations of gas dynamics for the basic conserved variables and an additional set of effective equations

for the problem-dependent material quantities. In this approach, as in its Cartesian coordinates counterpart (cf. [30, 31]), the latter equations are derived to ensure the correct fluid mixing when approximating the equations numerically with material interfaces, see Section 2. With the proposed model equations, accurate results can be obtained on a mapped grid using a standard method, such as the high-resolution wave propagation algorithm for a single-phase flow (cf. [8, 9, 21]), see Section 4 for numerical examples.

There are quite a few other numerical approaches available in the literature for approximating compressible multiphase problems over a multi-dimensional domain with complex geometries. Some representative ones are the overlapping grid method [5], the unstructured grid methods [2, 11, 43], and the Cartesian grid embedded boundary method [35].

An advantage of the mapped-grid approach described here is that extension of the method from two to three dimensions can be done in a straightforward manner for simple geometries such as cylinders, spheres, and their variants [9]. This is in contrast with the extension of an unstructured or a Cartesian grid method, where it requires a significant algorithmic and programming effort to realize each of the methods that are designed of general purpose. In addition to that, if we want to use a front tracking method to improve numerical resolution of shock waves and interfaces, with complex geometries involved, it would be relatively easier to apply the method on a body-fitted mapped grid than on a fixed Cartesian grid, see [17, 37] for an example. Furthermore, it is also easy to combine the method with a class of moving mesh techniques (cf. [38, 40]) for efficient solution adaptation.

It should be mentioned that the methodology we have given here is by no means limited to the current case with the stiffened gas equation of state. Extension of the method to problems involving more complicated equations of state can be made by considering, for instance, either a γ-based model of the author [32] or a α-based model of Allaire *et al.* [3] (see Section 2.2), and proceeding with the idea described in this paper. Without going into the details for that, our goal is to establish the basic solution strategy and validate its use via some sample numerical experimentations; this is a necessary step for our further development of the method towards more complicated problems of fundamental importance (cf. [15, 18, 27, 28] and references therein).

The format of this paper is as follows. In Section 2, we describe our mathematical model for a simplified homogeneous multiphase flow in curvilinear coordinates. In Section 3, we review briefly the wave propagation method on mapped grids. Numerical results of some sample test problems in two and

three dimensions are presented in Section 4.

2. Mathematical models in curvilinear coordinates

The basic governing equations in our mapped grid algorithm consist of two parts. We use the Euler equations in a curvilinear coordinate as a model system for the motion of the fluid mixtures of the conserved variables in a multiphase grid cell. With that, from the mass and energy conservations, we derive a set of effective equations for the problem-dependent material quantities in those cells, see below, that can be used directly to the determination of the pressure from the equation of state. Combining this two set of the equations together with the equation of state constitutes a complete mathematical model that is fundamental in our mapped grid algorithm for numerical approximation of multiphase flow problems with complex geometries.

To find out the aforementioned equations in a three-dimensional $N_d = 3$ curvilinear coordinate system, for example, we introduce a coordinate mapping from the physical domain (x_1, x_2, x_3) to the computational domain (ξ_1, ξ_2, ξ_3) via the relations

$$\begin{aligned} dx_1 &= a_1 d\xi_1 + a_2 d\xi_2 + a_3 d\xi_3, \\ dx_2 &= b_1 d\xi_1 + b_2 d\xi_2 + b_3 d\xi_3, \\ dx_3 &= c_1 d\xi_1 + c_2 d\xi_2 + c_3 d\xi_3, \end{aligned} \tag{3}$$

where a_i, b_i, c_i for $i = 1, 2, 3$ are the metric terms of the mapping. Then under this mapping, the Euler Eqs. (1) can be transformed into the new coordinate system as

$$\begin{aligned} &\frac{\partial \rho}{\partial t} + \frac{1}{J} \sum_{j=1}^{N_d} \frac{\partial}{\partial \xi_j} (\rho U_j) = 0, \\ &\frac{\partial}{\partial t} (\rho u_i) + \frac{1}{J} \sum_{j=1}^{N_d} \frac{\partial}{\partial \xi_j} (\rho u_i U_j + p J_{ji}) = 0, \quad i = 1, 2, \ldots, N_d, \\ &\frac{\partial E}{\partial t} + \frac{1}{J} \sum_{j=1}^{N_d} \frac{\partial}{\partial \xi_j} (E U_j + p U_j) = 0, \end{aligned} \tag{4}$$

where $U_j = \sum_{i=1}^{N_d} u_i J_{ji}$ is the contravariant velocity in the ξ_j-direction for $j = 1, 2, \ldots, N_d$. Here the quantities J_{ij} for $i, j = 1, 2, 3$ are as a consequence

of the coordinate transformation that satisfies the following expressions:

$$\begin{pmatrix} J_{11} & J_{12} & J_{13} \\ J_{21} & J_{22} & J_{23} \\ J_{31} & J_{32} & J_{33} \end{pmatrix} = \begin{pmatrix} b_2c_3 - b_3c_2 & a_3c_2 - a_2c_3 & a_2b_3 - a_3b_2 \\ b_3c_1 - b_1c_3 & a_1c_3 - a_3c_1 & a_3b_1 - a_1b_3 \\ b_1c_2 - b_2c_1 & a_2c_1 - a_1c_2 & a_1b_2 - a_2b_1 \end{pmatrix}, \tag{5}$$

and the quantity $J = \det |\partial(x_1, x_2, x_3)/\partial(\xi_1, \xi_2, \xi_3)|$ is the Jacobian of the mapping which can be computed by

$$J = \sum_{i=1}^{3} a_i J_{1i} = \sum_{i=1}^{3} b_i J_{2i} = \sum_{i=1}^{3} c_i J_{3i}. \tag{6}$$

Note that during the initialization step, all the coordinate transformation variables such as a_i, b_i, c_i, J_{1i}, J_{2i}, J_{3i} for $i = 1, 2, 3$, and J would be determined and remained fixed at all time when a mapped grid is constructed by a chosen numerical grid generator (cf. [9, 39]).

It is easy to see that (3) would be a two-dimensional coordinate mapping from (x_1, x_2) to (ξ_1, ξ_2) for any spatial location x_3 in the physical domain, if we have a simplified data set where the quantities a_3, b_3, c_1, and c_2 are all zero, and c_3 is equal to one. In this instance, if we set $N_d = 2$ in (4) with the coordinate transformation variables defined as in (5) and (6), we would have the same Euler equations in a two-dimensional curvilinear coordinate when a mapping of the form

$$\begin{aligned} dx_1 &= a_1 d\xi_1 + a_2 d\xi_2, \\ dx_2 &= b_1 d\xi_1 + b_2 d\xi_2, \end{aligned} \tag{7}$$

is used in the derivation (cf. [4, 7, 16, 42]). Thus, without causing any confusion, we may simply use the symbol N_d as in the Cartesian case, see (1), to represent the number of spatial dimension in the curvilinear-coordinate formulation of equations.

2.1. γ-based model equations

To derive the effective equations for the mixture of material quantities in curvilinear coordinates, one approach is to start with an interface-only problem (cf. [30, 32, 33, 34]) where both the pressure and each phase of the particle velocities are constant in the domain, while the other variables such as the density and the material quantities are having jumps across some

interfaces. Then, from (4), it is easy to obtain an equation for the time-dependent behavior of the total internal energy as

$$\frac{\partial}{\partial t}(\rho e) + \frac{1}{J}\sum_{j=1}^{N_d} U_j \frac{\partial}{\partial \xi_j}(\rho e) = 0.$$

Now, by inserting (2) into the above equation, we find an alternative form:

$$\frac{\partial}{\partial t}\left(\frac{p}{\gamma-1} - \frac{\rho-\rho_0}{\gamma-1}\mathcal{B}\right) + \frac{1}{J}\sum_{j=1}^{N_d} U_j \frac{\partial}{\partial \xi_j}\left(\frac{p}{\gamma-1} - \frac{\rho-\rho_0}{\gamma-1}\mathcal{B}\right) = 0, \quad (8)$$

that is in relation to not only the pressure, but also the density and the material quantities γ, ρ_0, and $\mathcal{B}$.

In our algorithm, to maintain the pressure in equilibrium as it should be for this interface-only problem and also to determine all the three material quantities in (2), we split (8) into the following three equations for the fluid mixture of $1/(\gamma-1)$, $\rho\mathcal{B}/(\gamma-1)$, and $\rho_0\mathcal{B}/(\gamma-1)$ as

$$\frac{\partial}{\partial t}\left(\frac{1}{\gamma-1}\right) + \frac{1}{J}\sum_{j=1}^{N_d} U_j \frac{\partial}{\partial \xi_j}\left(\frac{1}{\gamma-1}\right) = 0, \quad (9)$$

$$\frac{\partial}{\partial t}\left(\frac{\rho\mathcal{B}}{\gamma-1}\right) + \frac{1}{J}\sum_{j=1}^{N_d} U_j \frac{\partial}{\partial \xi_j}\left(\frac{\rho\mathcal{B}}{\gamma-1}\right) = 0, \quad (10)$$

$$\frac{\partial}{\partial t}\left(\frac{\rho_0\mathcal{B}}{\gamma-1}\right) + \frac{1}{J}\sum_{j=1}^{N_d} U_j \frac{\partial}{\partial \xi_j}\left(\frac{\rho_0\mathcal{B}}{\gamma-1}\right) = 0, \quad (11)$$

respectively. As before (cf. [31, 32, 33, 34]), since in practice we are interested in shock wave problems as well, we should take the equations, *i.e.*, (9), (10), and (11), in a form so that all the three material quantities remain unchanged across both shocks and rarefaction waves. In this regard, it is easy to see that with $1/(\gamma-1)$ and $\rho_0\mathcal{B}/(\gamma-1)$ governed in turn by (9) and (11), there is no problem to do so (cf. [1, 30]). For $\rho\mathcal{B}/(\gamma-1)$, however, due to the dependence of the density term, it turns out that, in a time when such a situation occurs, for consistent with the mass conservation law of the fluid mixture in (4), the primitive form of (10) should be modified by

$$\frac{\partial}{\partial t}\left(\frac{\rho\mathcal{B}}{\gamma-1}\right) + \frac{1}{J}\sum_{j=1}^{N_d} \frac{\partial}{\partial \xi_j}\left(\frac{\rho\mathcal{B}}{\gamma-1}U_j\right) = 0, \quad (12)$$

so that the mass-conserving property of the solution in the single phase region can be acquired also.

In summary, combining the Euler equations (4) and the set of effective equations: (9), (11), and (12), yields a so-called γ-based model system as

$$
\begin{aligned}
&\frac{\partial \rho}{\partial t}+\frac{1}{J}\sum_{j=1}^{N_d}\frac{\partial}{\partial \xi_j}\left(\rho U_j\right)=0,\\
&\frac{\partial}{\partial t}\left(\rho u_i\right)+\frac{1}{J}\sum_{j=1}^{N_d}\frac{\partial}{\partial \xi_j}\left(\rho u_i U_j+pJ_{ji}\right)=0,\quad i=1,2,\ldots,N_d,\\
&\frac{\partial E}{\partial t}+\frac{1}{J}\sum_{j=1}^{N_d}\frac{\partial}{\partial \xi_j}\left(EU_j+pU_j\right)=0,\\
&\frac{\partial}{\partial t}\left(\frac{1}{\gamma-1}\right)+\frac{1}{J}\sum_{j=1}^{N_d}U_j\frac{\partial}{\partial \xi_j}\left(\frac{1}{\gamma-1}\right)=0,\\
&\frac{\partial}{\partial t}\left(\frac{\rho_0\mathcal{B}}{\gamma-1}\right)+\frac{1}{J}\sum_{j=1}^{N_d}U_j\frac{\partial}{\partial \xi_j}\left(\frac{\rho_0\mathcal{B}}{\gamma-1}\right)=0,\\
&\frac{\partial}{\partial t}\left(\frac{\rho\mathcal{B}}{\gamma-1}\right)+\frac{1}{J}\sum_{j=1}^{N_d}\frac{\partial}{\partial \xi_j}\left(\frac{\rho\mathcal{B}}{\gamma-1}U_j\right)=0;
\end{aligned}
\tag{13}
$$

this gives us N_d+5 equations to be solved in total that is nicely independent of the number of fluid phases involved in the problem. With a system expressed in this way, there is no problem to compute all the state variables of interests, including the pressure from the equation of state

$$
p=\left[E-\frac{\sum_{i=1}^{N_d}(\rho u_i)^2}{2\rho}+\left(\frac{\rho\mathcal{B}}{\gamma-1}\right)-\left(\frac{\rho_0\mathcal{B}}{\gamma-1}\right)\right]\Big/\left(\frac{1}{\gamma-1}\right). \tag{14}
$$

For the ease of the latter discussion, it is useful to write (13) into a more compact expression by

$$
\frac{\partial q}{\partial t}+\frac{1}{J}\sum_{j=1}^{N_d}\left(\frac{\partial}{\partial \xi_j}f_j(q)+B_j(q)\frac{\partial q}{\partial \xi_j}\right)=0, \tag{15}
$$

with

$$
\begin{aligned}
q &= \left(\rho, \rho u_1, \ldots, \rho u_{N_d}, E, \frac{1}{\gamma-1}, \frac{\rho_0 \mathcal{B}}{\gamma-1}, \frac{\rho \mathcal{B}}{\gamma-1}\right)^T, \\
f_j &= \Bigg(\rho U_j, \rho u_1 U_j + p J_{j1}, \ldots, \rho u_{N_d} U_j + p J_{j,N_d}, E U_j + p U_j, \\
&\qquad 0, 0, \frac{\rho \mathcal{B}}{\gamma-1} U_j\Bigg)^T, \\
B_j &= \operatorname{diag}\left(0, 0, \ldots, 0, 0, U_j, U_j, 0\right),
\end{aligned}
\tag{16}
$$

for $j = 1, 2, \ldots, N_d$. Note that in the Cartesian coordinates case where the coordinate mapping quantities a_1, b_2, c_3 are all equal to one, while the remaining ones are all zeros, (15) reduces to

$$
\frac{\partial q}{\partial t} + \sum_{j=1}^{N_d} \left(\frac{\partial}{\partial x_j} \breve{f}_j(q) + \breve{B}_j(q) \frac{\partial q}{\partial x_j} \right) = 0, \tag{17}
$$

with $\breve{f}_j$ and $\breve{B}_j$ defined in turn by

$$
\begin{aligned}
\breve{f}_j &= \Bigg(\rho u_j, \rho u_1 u_j + p\delta_{1j}, \ldots, \rho u_{N_d} u_j + p\delta_{3j}, E u_j + p u_j, \\
&\qquad 0, 0, \frac{\rho \mathcal{B}}{\gamma-1} u_j\Bigg)^T, \\
\breve{B}_j &= \operatorname{diag}\left(0, 0, \ldots, 0, 0, u_j, u_j, 0\right),
\end{aligned}
\tag{18}
$$

Then it is easy to check that f_j and B_j are related to $\breve{f}_j$ and $\breve{B}_j$ via

$$
f_j = \sum_{i=1}^{N_d} \breve{f}_i J_{ji} \quad \text{and} \quad B_j = \sum_{i=1}^{N_d} \breve{B}_i J_{ji},
$$

respectively.

With these notations, by assuming the proper smoothness of the solutions, the quasi-linear form of our model (15) can be written as

$$
\frac{\partial q}{\partial t} + \frac{1}{J} \sum_{j=1}^{N_d} \left(A_j(q) + B_j(q)\right) \frac{\partial q}{\partial \xi_j} = 0, \tag{19}
$$

where $A_j = \partial f_j/\partial q = \sum_{i=1}^{N_d} \breve{A}_i J_{ji}$ is the Jacobian matrix of f_j with $\breve{A}_i = \partial \breve{f}_i/\partial q$ for $i = 1, 2, \ldots, N_d$. If we assume further that the thermodynamic description of the materials of interest is limited by the stability requirement, it is a straightforward matter to show that any linear combination of the matrices $\breve{A}_i + \breve{B}_i$ for $i = 1, 2, \ldots, N_d$ is diagonalizable with real eigenvalues and a complete set of linearly independent right eigenvectors (cf. [33]). Hence, we may conclude that our multiphase model is hyperbolic. Regarding discontinuous solutions of the system, such as shock waves or contact discontinuities, we find the usual form of the Rankine-Hugoniot jump conditions across the waves (cf. [13]).

2.2. α-based model equations

Before proceeding further, it should be mentioned that to define the initial fluid mixtures $1/(\gamma - 1)$, $\rho\mathcal{B}/(\gamma - 1)$, and $\rho_0\mathcal{B}/(\gamma - 1)$ in a grid cell that contains $M_f \geq 1$ different fluid phases where each of them occupies a distinct region with a volume-fraction function $\alpha_i \in [0, 1]$ in relation to it for $i = 1, 2, \ldots, M_f$, $\sum_{i=1}^{M_f} \alpha_i = 1$, we use the equation of state (2) of the form

$$\rho e = \sum_{i=1}^{M_f} \alpha_i \rho_i e_i = \sum_{i=1}^{M_f} \alpha_i \left(\frac{p_i}{\gamma_i - 1} - \frac{\rho_i - \rho_{0,i}}{\gamma_i - 1} \mathcal{B}_i \right) = \frac{p}{\gamma - 1} - \frac{\rho - \rho_0}{\gamma - 1} \mathcal{B}.$$

Here the subscript "i" denotes the state variable of fluid phase i. By taking a similar approach as employed in Section 2.1 for the derivation of the γ-based effective equations it comes out readily a splitting of the above expression into the relations:

$$\frac{1}{\gamma - 1} = \sum_{i=1}^{M_f} \frac{\alpha_i}{\gamma_i - 1}, \quad \frac{\rho\mathcal{B}}{\gamma - 1} = \sum_{i=1}^{M_f} \frac{\alpha_i \rho_i \mathcal{B}_i}{\gamma_i - 1}, \quad \frac{\rho_0\mathcal{B}}{\gamma - 1} = \sum_{i=1}^{M_f} \frac{\alpha_i \rho_{0,i} \mathcal{B}_i}{\gamma_i - 1}, \tag{20}$$

where in the process of splitting the terms we have imposed the condition

$$\frac{p}{\gamma - 1} = \sum_{i=1}^{M_f} \frac{\alpha_i p_i}{\gamma_i - 1}. \tag{21}$$

Clearly when each of the partial pressures is in an equilibrium state within a grid cell, in conjunction with the first part of (20), the pressure p obtained from (21) would remain in the same equilibrium as well, *i.e.*, $p = p_i$ for $i = 1, 2, \ldots, M_f$.

Now if the above volume-fraction notion of the states $1/(\gamma-1)$, $\rho\mathcal{B}/(\gamma-1)$, and $\rho_0\mathcal{B}/(\gamma-1)$ are being employed in the γ-based effective equations together with the usual definition of the mixture density $\rho=\sum_{i=1}^{M_f}\alpha_i\rho_i$, we are able to rewrite them straightforwardly into a componentwise form as

$$\frac{\partial}{\partial t}\left(\frac{\alpha_i}{\gamma_i-1}\right)+\frac{1}{J}\sum_{j=1}^{N_d}U_j\frac{\partial}{\partial\xi_j}\left(\frac{\alpha_i}{\gamma_i-1}\right)=0, \tag{22}$$

$$\frac{\partial}{\partial t}\left(\frac{\alpha_i\rho_i\mathcal{B}_i}{\gamma_i-1}\right)+\frac{1}{J}\sum_{j=1}^{N_d}\frac{\partial}{\partial\xi_j}\left(\frac{\alpha_i\rho_i\mathcal{B}_i}{\gamma_i-1}U_j\right)=0, \tag{23}$$

$$\frac{\partial}{\partial t}\left(\frac{\alpha_i\rho_{0,i}\mathcal{B}_i}{\gamma_i-1}\right)+\frac{1}{J}\sum_{j=1}^{N_d}U_j\frac{\partial}{\partial\xi_j}\left(\frac{\alpha_i\rho_{0,i}\mathcal{B}_i}{\gamma_i-1}\right)=0, \tag{24}$$

$i=1,2,\ldots,M_f$. Then based on the fact that all the material quantities γ_i, $\mathcal{B}_i$, and $\rho_{0,i}$ will be kept as a constant in each phase of the domain at all time, from (22) or (24) , it is easy to find the transport equation for the volume fraction α_i as

$$\frac{\partial\alpha_i}{\partial t}+\frac{1}{J}\sum_{j=1}^{N_d}U_j\frac{\partial\alpha_i}{\partial\xi_j}=0, \tag{25}$$

whereas, from (23), we find the conservation law for the phasic density $\alpha_i\rho_i$ as

$$\frac{\partial}{\partial t}\left(\alpha_i\rho_i\right)+\frac{1}{J}\sum_{j=1}^{N_d}\frac{\partial}{\partial\xi_j}\left(\alpha_i\rho_iU_j\right)=0. \tag{26}$$

It is apparent that, if the solutions of α_i and $\alpha_i\rho_i$ are known from the equations for $i=1,2,\ldots,M_f$, we may, therefore, compute $1/(\gamma-1)$, $\rho\mathcal{B}/(\gamma-1)$, and $\rho_0\mathcal{B}/(\gamma-1)$ directly according to (20). Thus, instead of using the γ-based effective equations, it is a viable alternate to use the α-based equations: (25) and (26), for the motion of the mixture of the material quantities of the problem.

To sum up, combining (25) and (26) with the momentum and energy equations in (4) yields a α-based (or called volume-fraction) model system

that can be written as

$$
\begin{aligned}
&\frac{\partial}{\partial t}\left(\alpha_i\rho_i\right)+\frac{1}{J}\sum_{j=1}^{N_d}\frac{\partial}{\partial\xi_j}\left(\alpha_i\rho_i U_j\right)=0,\quad i=1,2,\ldots,M_f\\
&\frac{\partial}{\partial t}\left(\rho u_i\right)+\frac{1}{J}\sum_{j=1}^{N_d}\frac{\partial}{\partial\xi_j}\left(\rho u_i U_j+pJ_{ji}\right)=0,\quad i=1,2,\ldots,N_d,\\
&\frac{\partial E}{\partial t}+\frac{1}{J}\sum_{j=1}^{N_d}\frac{\partial}{\partial\xi_j}\left(EU_j+pU_j\right)=0,\\
&\frac{\partial\alpha_i}{\partial t}+\frac{1}{J}\sum_{j=1}^{N_d}U_j\frac{\partial\alpha_i}{\partial\xi_j}=0,\quad i=1,2,\ldots,M_f-1;
\end{aligned}
\tag{27}
$$

this gives us totally $2M_f+N_d$ equations to be solved. Here analogously to (14) the pressure can be determined from the equation of state

$$
p=\left[E-\frac{\sum_{i=1}^{N_d}(\rho u_i)^2}{2\rho}+\sum_{i=1}^{M_f}\frac{\alpha_i\rho_i\mathcal{B}_i}{\gamma_i-1}-\sum_{i=1}^{M_f}\frac{\alpha_i\rho_{0,i}\mathcal{B}_i}{\gamma_i-1}\right]\Bigg/\sum_{i=1}^{M_f}\frac{\alpha_i}{\gamma_i-1},
$$

where we have assumed $\alpha_{M_f}=1-\sum_{i=1}^{M_f-1}\alpha_i$.

It is clear that (27) can be written of the form (15) in which we have q, f_j, and B_j defined by

$$
\begin{aligned}
q&=\left(\alpha_1\rho_1,\ldots,\alpha_{M_f}\rho_{M_f},\rho u_1,\ldots,\rho u_{N_d},E,\alpha_1,\ldots,\alpha_{M_f-1}\right)^T,\\
f_j&=\big(\alpha_1\rho_1U_j,\ldots,\alpha_{M_f}\rho_{M_f}U_j,\rho u_1U_j+pJ_{j1},\ldots,\rho u_{N_d}U_j+pJ_{j,N_d},\\
&\qquad EU_j+pU_j,0,\ldots,0\big)^T,\\
B_j&=\operatorname{diag}\left(0,\ldots,0,\ldots,0,U_j,\ldots,U_j\right).
\end{aligned}
$$

In a similar manner, in the Cartesian coordinates case where the system is of the form (17), we have $\breve{f}_j$ and $\breve{B}_j$ defined by

$$
\begin{aligned}
\breve{f}_j&=\big(\alpha_1\rho_1u_j,\ldots,\alpha_{M_f}\rho_{M_f}u_j,\rho u_1u_j+p\delta_{j1},\ldots,\rho u_{N_d}u_j+p\delta_{j,N_d},\\
&\qquad Eu_j+pu_j,0,\ldots,0\big)^T,\\
\breve{B}_j&=\operatorname{diag}\left(0,\ldots,0,\ldots,0,u_j,\ldots,u_j\right).
\end{aligned}
$$

We note that since the derivation of the α-based model follows closely to the γ-based model, it can be shown that this model is hyperbolic also (cf. [3]

for the Cartesian coordinates case) and is as effective as the γ-based model for multiphase flow problems with the stiffened gas equation of state. But for problems with $M_f \geq 3$, the γ-based model is a prefer one to use, because the basic equations for the model stay as $N_d + 5$, see (13), irrespective of the number of fluid phases involved in the problem.

2.3. Include source terms

To end this section, we comment that if x_1 is the axisymmetric direction, an axisymmetric version of our multiphase models in two dimensions can be written as

$$\frac{\partial q}{\partial t} + \frac{1}{J}\sum_{j=1}^{2}\left(\frac{\partial}{\partial \xi_j} f_j(q) + B_j(q)\frac{\partial q}{\partial \xi_j}\right) = \psi(q), \tag{28}$$

where ψ is the source term derived directly from the geometric simplification. That is, we find

$$\psi = -\frac{1}{x_1}\left(\rho u_1, \rho u_1^2, \rho u_1 u_2, E u_1 + p u_1, 0, 0, \frac{\rho \mathcal{B}}{\gamma - 1} u_1\right)^T, \tag{29}$$

when the γ-based model is considered, and have

$$\psi = -\frac{1}{x_1}\left(\alpha_1\rho_1 u_1, \ldots, \alpha_{M_f}\rho_{M_f} u_{M_f}, \rho u_1^2, \rho u_1 u_2, E u_1 + p u_1, 0, \ldots, 0\right)^T,$$

when the α-based model is considered. In addition to that, if gravity is the only body force in the problem formulation, in the γ-based model, for example, we may add in the following source term:

$$\psi = -\left(0, 0, \rho g, \rho g u_2, 0, 0, 0\right)^T$$

as well. Here g denotes the gravitational constant. As to the other source terms such as the one arise from the surface tension force at the interface, we may use a continuum surface force model of Brackbill *et al.* [6] for that, see the work done by Perigaud and Saurel [26] and the references therein for more details. Since it is beyond the scope of this paper, we will not discuss this further.

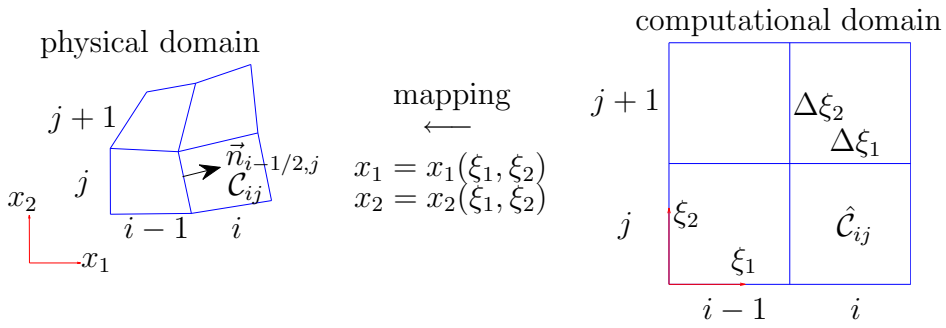

Figure 1: A sample grid system in our two-dimensional numerical method on a quadrilateral grid. The numerical solution on the rectangular grid cell $\hat{\mathcal{C}}_{ij}$ in the computational domain gives distinctively the result on the mapped quadrilateral grid cell $\mathcal{C}_{ij}$ in the physical domain for all the grid cell (i, j).

3. Numerical approximation on mapped grids

We use a state-of-the-art finite volume method in wave-propagation form (cf. [9, 21]) for the numerical discretization of our multiphase flow models (without the source terms) on mapped grids. The method is based on solving one-dimensional Riemann problems at each cell edge, and the waves (*i.e.*, discontinuities moving at constant speeds) arising from the Riemann problem are employed to update the cell averages in the cells neighboring each edge.

To review the basic idea of the method, we consider the two-dimensional quadrilateral grid case as illustrated in Fig. 1, for example. In a finite volume method, the approximate value of the cell average of the solution q over the (i, j)th grid cell at a time t_n can be written as

$$Q_{ij}^n \approx \frac{1}{\mathcal{M}(\mathcal{C}_{ij})} \int_{\mathcal{C}_{ij}} q(x_1, x_2, t_n)\, dx_1 dx_2 = \frac{1}{\kappa_{ij}\Delta\xi_1\Delta\xi_2} \int_{\hat{\mathcal{C}}_{ij}} q(\xi_1, \xi_2, t_n)\, d\xi_1 d\xi_2,$$

where $\mathcal{C}_{ij}$ and $\hat{\mathcal{C}}_{ij}$ denote the regions occupied by the grid cell (i, j) in the physical and computational domains, respectively, and $\mathcal{M}(\mathcal{C}_{ij}) = \kappa_{ij}\Delta\xi_1\Delta\xi_2$ is the measure (area) of $\mathcal{C}_{ij}$. Here $\kappa_{ij} = J(\mathcal{C}_{ij})$ is the Jacobian of the mapping of this cell, and $\Delta\xi_k$ is the mesh size in the ξ_k-direction of the computational domain for $k = 1, 2$. The time step from the current time t_n to the next t_{n+1} is denoted by Δt.

In this setup, a fully discrete version of the wave propagation method for the equations (15) is a Godunov-type scheme on a quadrilateral grid that

can be written as

$$Q_{ij}^{n+1} = Q_{ij}^{n} - \frac{1}{\kappa_{ij}} \frac{\Delta t}{\Delta \xi_1} \left(\mathcal{A}_1^+ \Delta Q_{i-1/2,j} + \mathcal{A}_1^- \Delta Q_{i+1/2,j} \right) - \frac{1}{\kappa_{ij}} \frac{\Delta t}{\Delta \xi_2} \left(\mathcal{A}_2^+ \Delta Q_{i,j-1/2} + \mathcal{A}_2^- \Delta Q_{i,j+1/2} \right). \tag{30}$$

Here $\mathcal{A}_1^+ \Delta Q_{i-1/2,j}$, $\mathcal{A}_1^- \Delta Q_{i+1/2,j}$, $\mathcal{A}_2^+ \Delta Q_{i,j-1/2}$, and $\mathcal{A}_2^- \Delta Q_{i,j+1/2}$ are the right-, left-, up-, and down-moving fluctuations, respectively, that are entering into the grid cell. To determine these fluctuations, we need to solve the one-dimensional Riemann problems normal to the cell edges.

3.1. Computing fluctuations

Considering the fluctuations $\mathcal{A}_1^{\pm} \Delta Q_{i-1/2,j}$ arising from the edge $(i-1/2, j)$ between cells $(i-1, j)$ and (i, j), for example. This amounts to solve a Cauchy problem in the ξ_1-direction that consists of

$$\frac{\partial q}{\partial t} + \frac{1}{J} \frac{\partial f_1(q)}{\partial \xi_1} + B_1(q) \frac{1}{J} \frac{\partial q}{\partial \xi_1} = 0,$$

as for the equations and the piecewise constant data

$$q(\xi_1, \xi_2, t_n) = \begin{cases} Q_{i-1,j}^n & \text{if} \quad \xi_1 < (\xi_1)_{i-1/2} \\ Q_{ij}^n & \text{if} \quad \xi_1 > (\xi_1)_{i-1/2}, \end{cases}$$

as for the initial condition at a time t_n. As an example, we describe next the case for the γ-based model (13) in more details, and that the case for the α-based model (27) can be constructed in an analogous manner.

Let $\vec{n}_{i-1/2,j} = (\hat{b}_2, -\hat{a}_2)_{i-1/2,j}$ and $\vec{t}_{i-1/2,j} = (\hat{a}_2, \hat{b}_2)_{i-1/2,j}$ be the unit normal and tangential vectors to the cell edge $(i-1/2, j)$ in the physical grid, where $\hat{a}_i = a_i/S_i$ and $\hat{b}_i = b_i/S_i$ are the scaled version of the metric elements a_i and b_i in (7) with $S_i = \sqrt{a_i^2 + b_i^2}$ for $i = 1, 2$. Then to compute $\mathcal{A}_1^{\pm} \Delta Q_{i-1/2,j}$, as in [9, 21], we perform the following steps:

(1) Transform the data $Q_{i-1,j}^n$ and $Q_{i,j}^n$ into the new data $\breve{Q}_L$ and $\breve{Q}_R$ via

$$\breve{Q}_L = \mathcal{R}_{i-1/2,j} Q_{i-1,j}^n, \quad \breve{Q}_R = \mathcal{R}_{i-1/2,j} Q_{i,j}^n.$$

Here $\mathcal{R}_{i-1/2,j}$ is a rotation matrix defined by

$$\mathcal{R}_{i-1/2,j} = \begin{pmatrix} 1 & 0 & 0 & 0 \\ 0 & (\hat{b}_2)_{i-1/2,j} & -(\hat{a}_2)_{i-1/2,j} & 0 \\ 0 & (\hat{a}_2)_{i-1/2,j} & (\hat{b}_2)_{i-1/2,j} & 0 \\ 0 & 0 & 0 & I \end{pmatrix}$$

with I in it as being a 4×4 identity matrix. Clearly this rotation matrix rotates the velocity components of Q into components normal and tangential to the cell edge, and leaves the remaining components unchanged.

(2) Solve Riemann problem in the "x_1" direction for

$$\frac{\partial q}{\partial t} + \frac{\partial}{\partial x_1}\breve{f}_1(q) + \breve{B}_1(q)\frac{\partial q}{\partial x_1} = 0 \tag{31}$$

with $\breve{f}_1$ and $\breve{B}_1$ defined by (18) and the Riemann data $\breve{Q}_L$ and $\breve{Q}_R$. When an approximate Riemann solver is used for the numerical resolution, this would result in three propagating discontinuities that are moving with speeds $\breve{\lambda}^{1,k}_{i-1/2,j}$ and the jumps $\breve{\mathcal{W}}^{1,k}_{i-1/2,j}$ across each of them for $k = 1, 2, 3$, see [31, 33, 34] for an example.

(3) Define scaled speeds

$$\lambda^{1,k}_{i-1/2,j} = (S_2)_{i-1/2,j}\breve{\lambda}^{1,k}_{i-1/2,j}$$

and rotate jumps back to the Cartesian coordinates by

$$\mathcal{W}^{1,k}_{i-1/2,j} = \mathcal{R}^T_{i-1/2,j}\breve{\mathcal{W}}^{1,k}_{i-1/2,j}$$

for $k = 1, 2, 3$.

(4) Determine the left- and right-moving fluctuations in the form

$$\mathcal{A}_1^{\pm}\Delta Q_{i-1/2,j} = \sum_{k=1}^{3}\left(\lambda^{1,k}_{i-1/2,j}\right)^{\pm}\mathcal{W}^{1,k}_{i-1/2,j}.$$

As usual, the notations for the quantities $\lambda^{\pm}$ are set by $\lambda^+ = \max(\lambda, 0)$ and $\lambda^- = \min(\lambda, 0)$.

In a similar manner, we may determine the up- and down-moving fluctuations at the edge $(i, j-1/2)$ in the form

$$\mathcal{A}_2^{\pm}\Delta Q_{i,j-1/2} = \sum_{k=1}^{3}\left(\lambda^{2,k}_{i,j-1/2}\right)^{\pm}\mathcal{W}^{2,k}_{i,j-1/2}$$

that is as the result of solving

$$\frac{\partial q}{\partial t} + \frac{1}{J}\frac{\partial f_2(q)}{\partial \xi_2} + B_2(q)\frac{1}{J}\frac{\partial q}{\partial \xi_2} = 0$$

with the initial data $Q^n_{i,j-1}$ and $Q^n_{i,j}$.

3.2. High resolution corrections

To achieve high resolution (*i.e.*, second-order accurate on smooth solutions, and sharp and monotone profiles on discontinuous solutions), the speeds and the limited version of the jumps are used to construct the piecewise linear correction terms as before (cf. [21]), and are added to (30) in flux difference form as

$$Q_{ij}^{n+1} := Q_{ij}^{n+1} - \frac{1}{\kappa_{ij}}\frac{\Delta t}{\Delta \xi_1}\left(\widetilde{\mathcal{F}}^1_{i+1/2,j} - \widetilde{\mathcal{F}}^1_{i-1/2,j}\right) - \frac{1}{\kappa_{ij}}\frac{\Delta t}{\Delta \xi_2}\left(\widetilde{\mathcal{F}}^2_{i,j+1/2} - \widetilde{\mathcal{F}}^2_{i,j-1/2}\right).$$

Here at the edge $(i-1/2, j)$ the correction flux takes the form

$$\widetilde{\mathcal{F}}^1_{i-1/2,j} = \frac{1}{2}\sum_{k=1}^{3}\left|\lambda^{1,k}_{i-1/2,j}\right|\left(1 - \frac{\Delta t}{\kappa_{i-1/2,j}\Delta\xi_1}\left|\lambda^{1,k}_{i-1/2,j}\right|\right)\widetilde{\mathcal{W}}^{1,k}_{i-1/2,j},$$

and analogously at the edge $(i, j-1/2)$ the correction flux has the form

$$\widetilde{\mathcal{F}}^2_{i,j-1/2} = \frac{1}{2}\sum_{k=1}^{3}\left|\lambda^{2,k}_{i,j-1/2}\right|\left(1 - \frac{\Delta t}{\kappa_{i,j-1/2}\Delta\xi_2}\left|\lambda^{2,k}_{i,j-1/2}\right|\right)\widetilde{\mathcal{W}}^{2,k}_{i,j-1/2},$$

where $\kappa_{i-1/2,j} = (\kappa_{i-1,j} + \kappa_{i,j})/2$ and $\kappa_{i,j-1/2} = (\kappa_{i,j-1} + \kappa_{i,j})/2$. The quantity $\widetilde{\mathcal{W}}^{m,k}$ is a limited value of $\mathcal{W}^{m,k}$ obtained by comparing $\mathcal{W}^{m,k}$ with the corresponding $\mathcal{W}^{m,k}$ from the neighboring Riemann problem to the left (if $\lambda^{m,k} > 0$) or to the right (if $\lambda^{m,k} < 0$) for $m = 1, 2$ and $k = 1, 2, 3$.

In addition to that, a transverse propagation of wave is also included in the method as a part of the high-resolution correction terms. Here the right-moving fluctuation $\mathcal{A}_1^+\Delta Q_{i-1/2,j}$, for instance, is decomposed into transverse fluctuations $\mathcal{A}_2^\pm\mathcal{A}_1^+\Delta Q_{i-1/2,j}$ which can be used to update the solutions above and below cell (i, j). In a similar manner, the left-moving fluctuation $\mathcal{A}_1^-\Delta Q_{i-1/2,j}$ is split into $\mathcal{A}_2^\pm\mathcal{A}_1^-\Delta Q_{i-1/2,j}$ which are used to update the solutions above and below cell $(i-1, j)$, see [21] for the details.

With the transverse wave propagation, the method is typically stable as long as the time step Δt satisfies a variant of the CFL (Courant-Friedrichs-Lewy) condition of the form

$$\nu = \Delta t \max_{i,j,k}\left(\frac{\left|\lambda^{1,k}_{i-1/2,j}\right|}{\kappa_{i_p,j}\Delta\xi_1}, \frac{\left|\lambda^{2,k}_{i,j-1/2}\right|}{\kappa_{i,j_p}\Delta\xi_2}\right) \le 1, \tag{32}$$

where $i_p = i$ if $\lambda^{1,k}_{i-1/2,j} > 0$ and $i-1$ if $\lambda^{1,k}_{i-1/2,j} < 0$; j_p is defined analogously (cf. [40]). Furthermore, by following the basic steps discussed in [9, 21], it can be shown that the method is quasi-conservative in the sense that when applying the method to our multiphase model (15) not only the conservation laws but also the transport equations are approximated in a consistent manner by the method.

3.3. Three-dimensional extension

To extend this mapped grid method from two to three space dimensions, we use hexahedral meshes in place of quadrilateral grid cells, see Fig. 11 for an example. We use the fluctuation form of the method as usual in three dimensions for the solution updates that is an easy generalization of the three-dimensional wave propagation method on Cartesian grids proposed by Langseth and LeVeque [19] and also the two-dimensional method on mapped grid [21]. To implement the method, it is useful to make reference to the CLAWPACK webpage, see [9, 36] in particular, for the programming details. In Section 4.2, we present some sample results that show the feasibility of this method to practical compressible multiphase problems.

4. Numerical results

We now present numerical results to validate our mapped grid algorithm for compressible multiphase flow problems in two and three dimensions. Note that in this section we have only present solutions obtained using the γ-based model (13) to the method. This is because we have found a little difference between the results as compared to the ones using the α-based model (27) to the method for simulations.

4.1. Two-dimensional case

4.1.1. Smooth vortex flow

We begin our tests by performing a convergence study of the computed solutions for a two-dimensional vortex evolution problem (cf. [12, 29, 43]) that shows the order of accuracy that is attained for our high resolution method as the mesh is refined. In this problem, we assume a single-phase ideal gas flow with $\gamma = 1.4$ and $\mathcal{B} = 0$ in the stiffened gas equation of state (2). Initially, over a square domain of size $[0, 10] \times [0, 10]$, the state variables for the vortex

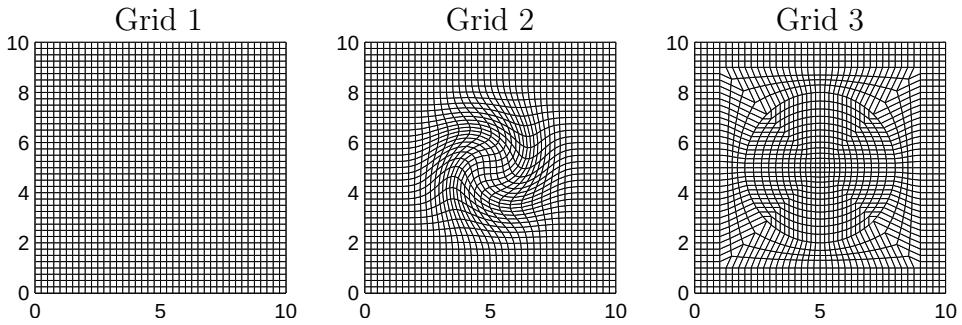

Figure 2: Three types of grids used for the smooth vortex flow problem.

are set by

$$\begin{aligned}
\rho &= \left(1 - \frac{(\gamma-1)\epsilon^2}{8\gamma\pi^2}\exp\left(1-r^2\right)\right)^{1/(\gamma-1)}, \\
p &= \rho^\gamma, \\
u_1 &= 1 - \frac{\epsilon}{2\pi}\exp\left((1-r^2)/2\right)(x_2-\bar{x}_2), \\
u_2 &= 1 + \frac{\epsilon}{2\pi}\exp\left((1-r^2)/2\right)(x_1-\bar{x}_1),
\end{aligned}$$

where $r = \sqrt{(x_1-\bar{x}_1)^2 + (x_2-\bar{x}_2)^2}$ is the distance between points (x_1, x_2) and the vortex center $(\bar{x}_1, \bar{x}_2) = (5, 5)$, and $\epsilon = 5$ is the vortex strength. Note that the above states are as the results of an isentropic perturbation in p/ρ, u_1, and u_2 to the mean flow with $\bar{\rho} = 1$, $\bar{p} = 1$, $\bar{u}_1 = 1$, and $\bar{u}_2 = 1$, and it is known that with the periodic conditions in both the x_1- and x_2-direction the exact solution for this problem is simply the passive motion of a smooth vortex by the mean flow velocity.

We compare the behavior of the high-resolution wave propagation method described in Section 3 on three different types of grids as illustrated in Fig. 2:

Grid 1: Cartesian grids with square grid cells,
Grid 2: Quadrilateral grids of the type described in [10],
Grid 3: Quadrilateral grids of the type described in [9],

see [22] for a similar computation on the transport of a scalar quantity in a divergence-free velocity field. In order to estimate the order of accuracy of the method, for each grid type, we compute the solution at the mesh refinement sequence: $\Delta\xi_1^{(i)} = \Delta\xi_2^{(i)} = \Delta\xi^{(i)} = 1/2^{(i+2)}$ for $i = 0, 1, 2, 3$, *i.e.*, by using an

$N \times N$ grid for $N = 40$, 80, 160 and 320. To ensure that our convergence study is not adversely affected by a loss of accuracy near local extrema in the solution, there is no limiter being used in the computations. In addition, the Courant number $\nu = 0.9$ defined by (32), and the Roe approximate Riemann solver are employed in the tests.

Numerical results at time $t = 10$ obtained from all the 12 tests are presented in Tables 1-3. Here $\mathcal{E}_1(z)$ and $\mathcal{E}_m(z)$ denote in turn the sequence of the 1- and maximum-norm error of the cell-average solution in z to the true solution at the cell center for $z = \rho, u_1, u_2$, and p. We estimate the rate of convergence using the errors on two consecutive grids based on the formula

$$\text{convergence order} = \ln\left(\frac{\mathcal{E}_k^{(i-1)}(z)}{\mathcal{E}_k^{(i)}(z)}\right) \Big/ \ln\left(\frac{\Delta\xi^{(i-1)}}{\Delta\xi^{(i)}}\right)$$

for $k = 1, m$ and $i = 1, 2, 3$.

From the tables, we observe that the method is second order accurate in most cases on this problem. It is important to note that the error behavior of the method on Grid 2 is on the same order of magnitude on Grid 1, the Cartesian grid, while this is not the case on Grid 3 which is a less smooth grid as compared to Grid 2. This indicates that the use of a smooth grid in a mapped grid method can indeed give a better resolution of the solution.

4.1.2. Passive interface evolution

We are next concerned with an interface only problem that the exact solution consists of a circular water column evolving in the air with uniform equilibrium pressure $\bar{p} = 10^5$Pa and constant particle velocity $(\bar{u}_1, \bar{u}_2) = (10^3, 10^3)$m/s throughout a quarter annulus domain. Here we take the initial condition that inside the column of radius $r_0 = 0.2$m about the center $(\bar{x}_1, \bar{x}_2) = (0.8, 0.8)$m the fluid is water with the data

$$(\rho, \gamma, \rho_0, \mathcal{B})_{r \le r_0} = \left(10^3\text{kg/m}^3, 4.4, 10^3\text{kg/m}^3, 2.64 \times 10^6(\text{m/s})^2\right),$$

while outside the column the fluid is air with the data

$$(\rho, \gamma, \rho_0, \mathcal{B})_{r > r_0} = \left(1.2\text{kg/m}^3, 1.4, 1.2, 0\right).$$

Note that despite the simplicity of the solution structure, this problem is one of the popular tests for the numerical validation of a compressible multiphase flow solver (cf. [30, 43]).

Table 1: High-resolution results for the smooth vortex test on Grid 1; 1- and maximum-norm errors in primitive variables are shown.

N	$\mathcal{E}_1(\rho)$	Order	$\mathcal{E}_1(u_1)$	Order	$\mathcal{E}_1(u_2)$	Order	$\mathcal{E}_1(p)$	Order
40	0.6673		2.3443		1.7121		0.8143	
80	0.1792	1.90	0.6194	1.92	0.4378	1.97	0.2128	1.94
160	0.0451	1.99	0.1537	2.01	0.1104	1.99	0.0536	1.99
320	0.0113	2.00	0.0384	2.00	0.0276	2.00	0.0134	2.00

N	$\mathcal{E}_m(\rho)$	Order	$\mathcal{E}_m(u_1)$	Order	$\mathcal{E}_m(u_2)$	Order	$\mathcal{E}_m(p)$	Order
40	0.1373		0.3929		0.1810		0.1742	
80	0.0377	1.87	0.1014	1.95	0.0502	1.85	0.0482	1.85
160	0.0093	2.02	0.0248	2.03	0.0123	2.03	0.0119	2.02
320	0.0022	2.07	0.0062	2.00	0.0030	2.04	0.0029	2.04

Table 2: High-resolution results for the smooth vortex test on Grid 2; 1- and maximum-norm errors in primitive variables are shown.

N	$\mathcal{E}_1(\rho)$	Order	$\mathcal{E}_1(u_1)$	Order	$\mathcal{E}_1(u_2)$	Order	$\mathcal{E}_1(p)$	Order
40	0.9298		2.6248		2.1119		1.2104	
80	0.2643	1.81	0.7258	1.85	0.5296	2.00	0.3277	1.89
160	0.0674	1.97	0.1833	1.99	0.1309	2.02	0.0845	1.96
320	0.0169	2.00	0.0458	2.00	0.0327	2.00	0.0212	1.99

N	$\mathcal{E}_m(\rho)$	Order	$\mathcal{E}_m(u_1)$	Order	$\mathcal{E}_m(u_2)$	Order	$\mathcal{E}_m(p)$	Order
40	0.1676		0.4112		0.2259		0.2111	
80	0.0471	1.83	0.1242	1.73	0.0645	1.79	0.0586	1.85
160	0.0126	1.91	0.0333	1.90	0.0162	2.02	0.0149	1.97
320	0.0033	1.93	0.0085	1.97	0.0040	2.00	0.0038	1.98

Table 3: High-resolution results for the smooth vortex test on Grid 3; 1- and maximum-norm errors in primitive variables are shown.

N	$\mathcal{E}_1(\rho)$	Order	$\mathcal{E}_1(u_1)$	Order	$\mathcal{E}_1(u_2)$	Order	$\mathcal{E}_1(p)$	Order
40	4.8272		4.7734		5.3367		5.4717	
80	1.5740	1.62	1.5633	1.61	1.5660	1.77	1.5634	1.81
160	0.4536	1.79	0.4559	1.78	0.4537	1.79	0.4560	1.78
320	0.1215	1.90	0.1221	1.90	0.1222	1.89	0.1221	1.90

N	$\mathcal{E}_m(\rho)$	Order	$\mathcal{E}_m(u_1)$	Order	$\mathcal{E}_m(u_2)$	Order	$\mathcal{E}_m(p)$	Order
40	0.4481		0.4475		0.4765		0.4817	
80	0.1170	1.94	0.1181	1.92	0.1196	1.99	0.1191	2.02
160	0.0434	1.43	0.0431	1.45	0.0442	1.43	0.0440	1.44
320	0.0117	1.89	0.0119	1.86	0.0119	1.89	0.0118	1.89

To discretize this quarter-annulus region, we use polar coordinates:

$$x_1(\xi_1, \xi_2) = \xi_1 \cos(\xi_2),$$
$$x_2(\xi_1, \xi_2) = \xi_1 \sin(\xi_2),$$

for $0.5\text{m} \leq \xi_1 \leq 2.5\text{m}$ and $0 \leq \xi_2 \leq \pi/2$, see Chapter 23 of [21] for an illustration. Figure 3 shows numerical results of the density and pressure at time $t = 520\mu$s obtained using our algorithm with the MINMOD limiter and the Roe solver on a 100×100 polar grid. From the 3D surface plot and the cross-section plot (along $\xi_2 = \pi/4$) of the density, we observe that the water column retains its circular shape and appears to be very well located also. From the 3D surface plot of the pressure and the scatter plot the relative error of the pressure, we find the computed pressure remains in the correct equilibrium state $\bar{p}$ (to be more accurate, the difference of these two is only on the order of machine epsilon), without any spurious oscillations near the air-water interface. Here, we use non-reflecting boundary conditions on all sides of the quarter annulus, while carrying out the computations.

4.1.3. Moving cylindrical vessel

Our next example concerns a moving cylindrical vessel problem studied by Banks *et al.* [5] in that inside the circle of radius $r_0 = 0.8$ about the

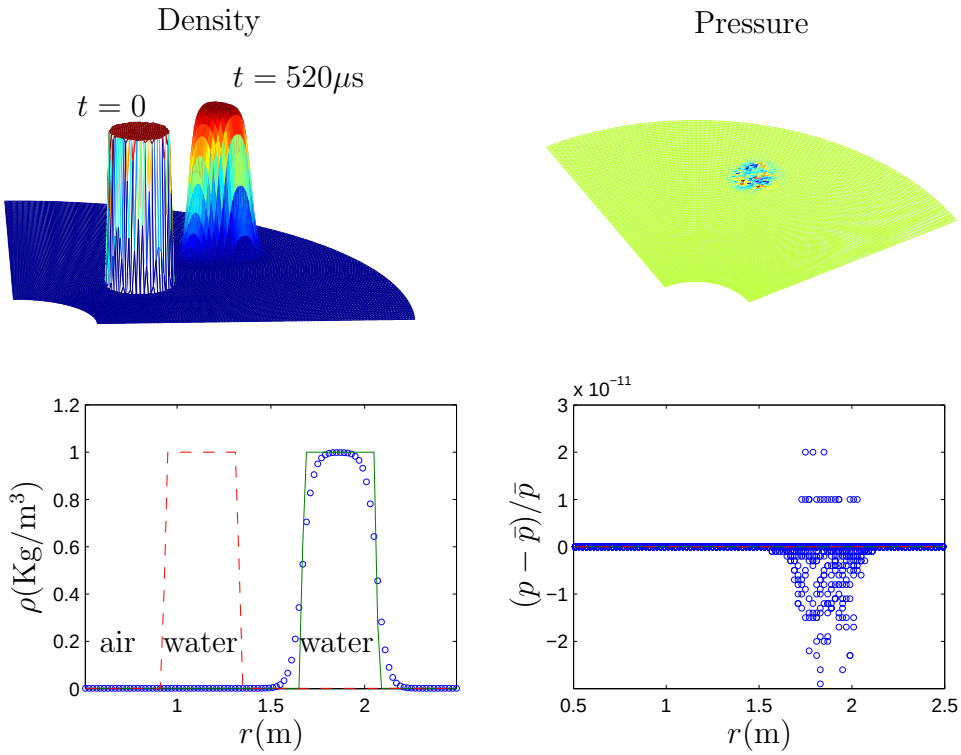

Figure 3: Numerical results for an interface only problem in a quarter annulus at time $t = 520\mu$s. On the top, surface plots of the density and pressure are shown, and on the bottom, cross-sectional plot (along the line $\xi_2 = \pi/4$) of the density and scatter plots of the relative error of the pressure are displayed, respectively. Here the solid line is the exact solution, and the dashed line is the initial condition at the time $t = 0$.

origin, there is a planar material interface located initially at $x_1 = 0$ that separates air on the left with the state variables

$$(\rho, u_1, u_2, p, \gamma, \rho_0, \mathcal{B}) = (1, -1, 0, 1, 1.4, 1, 0)\,,$$

and helium on the right with the state variables

$$(\rho, u_1, u_2, p, \gamma, \rho_0, \mathcal{B}) = (0.138, -1, 0, 1, 1.67, 0.138, 0)\,.$$

Note that in this set up we have imposed a uniform flow velocity $(u_1, u_2) = (-1, 0)$ throughout the domain, and so we are in the frame of the vessel moving with speed one in the x_1-direction.

To find an approximate solution of this problem, we use a a mapped grid approach proposed by Calhoun *et al.* [9] in that a grid point (ξ_1, ξ_2) in the

computational domain $[-1,1] \times [-1,1]$ is mapped to a grid point (x_1, x_2) in the circular domain by some simple algebraic rules, see Fig. 4 for an illustration. Numerical Schlieren images and pseudo-color plots of pressure are shown in Fig. 4 at four different times $t = 0.25$, 0.5, 0.75, and 1.0, where a 800×800 grid is used in the run. From the figure, it is easy to see that due to the impulsive motion of the vessel a rightward-going shock wave and a leftward-going rarefaction wave emerge from the left- and right-side boundary, respectively. Subsequently, these two waves would be interacting with the material interface that leads to collision of various transmitted and reflected waves. When we compare our results with those ones appeared in the literature (cf. [5, 43]), as far as the global wave structures are concerned, we notice good qualitative agreement of the solutions.

To check the quantitative information of our computed solutions, Fig. 5 compares the cross-sectional results for the same run along the circular boundary with those obtained using a wave-propagation based Cartesian grid embedded boundary method (cf. [20, 35, 37]). The close agreement between the mapped grid and Cartesian grid results in the shock waves and material interfaces are clearly observed.

4.1.4. Shock-bubble interaction in a nozzle

As an example to show how our algorithm works on shock waves in a more general two-dimensional geometry, we are interested in a shock-bubble interaction problem in a nozzle. For this problem, the shape of the nozzle is described by a flat curve

$$x_2^t = 1\text{m}$$

on the top, and by the witch of Agnesi

$$x_2^b(x_1) = \frac{8a^3}{x_1^2 + 4a^2}$$

on the bottom for $a = 0.2$m and $-2\text{m} \le x_1 \le 3\text{m}$. We use the initial condition that is composed of a planarly rightward-going Mach 1.422 shock wave located at $x_1 = -1.8$m in liquid traveling from left to right, and a stationary gas bubble of radius $r_0 = 0.2$m and center $(\bar{x}_1, \bar{x}_2) = (-1, 0.5)$m in the front of the shock wave. Inside the gas bubble, we have the data

$$(\rho, u_1, u_2, p) = \left(1.2\text{kg/m}^3, 0, 0, 10^5\text{Pa}\right),$$

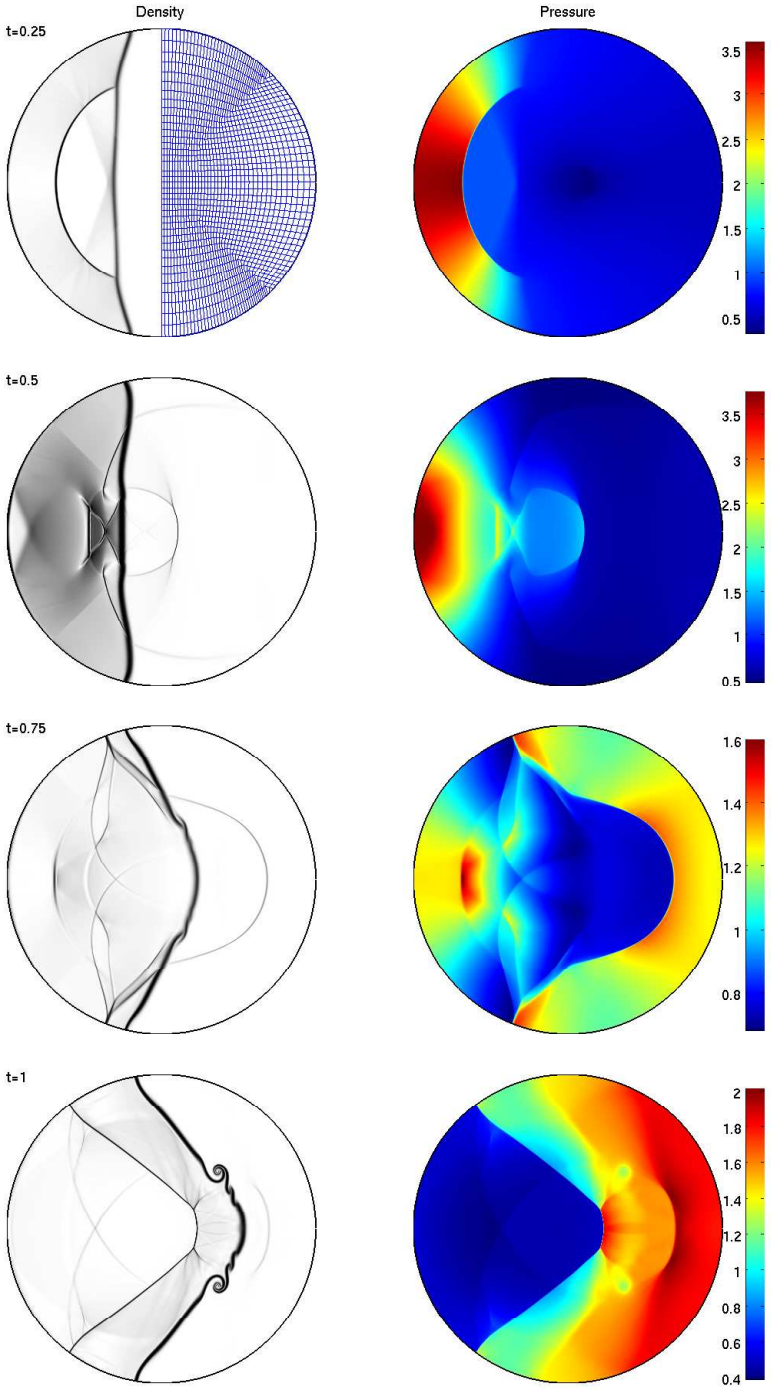

Figure 4: Numerical Schlieren images (on the left) and pseudo colors of pressure (on the right) for an impulsively driven cylinder containing an air-helium material interface. Solutions from top to bottom are at times $t = 0.25$, 0.5, 0.75, and 1.0.

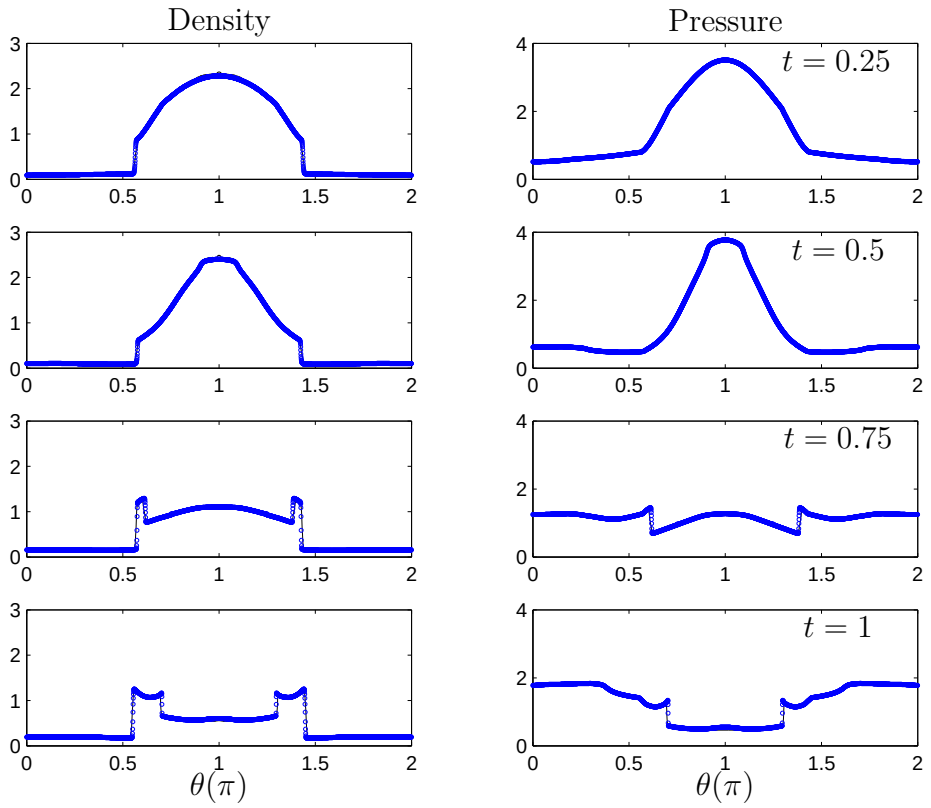

Figure 5: Cross-sectional plots of the results for the moving vessel run shown in Fig. 4 along the circular boundary, where the solid lines are results obtained using a Cartesian grid embedded boundary method [35] with the same grid size.

while outside the gas bubble where the fluid is liquid, we have the preshock state

$$(\rho, u_1, u_2, p) = \left(10^3 \text{kg/m}^3, 0, 0, 10^5 \text{Pa}\right),$$

and the postshock state

$$(\rho, u_1, u_2, p) = \left(1.23 \times 10^3 \text{kg/m}^3, 432.69 \text{m/s}, 0, 10^9 \text{Pa}\right).$$

Here the material-dependent parameters $(\gamma, \rho_0, \mathcal{B})$ for the gas- and liquid-phase are taken as $(1.4, 1.2\text{kg/m}^3, 0)$ and $(4.4, 10^3\text{kg/m}^3, 2.64 \times 10^6(\text{m/s})^2)$, respectively.

In carrying out the computation, we consider a body-fitted quadrilateral grid with the mapping function

$$\begin{aligned} x_1(\xi_1, \xi_2) &= \xi_1, \\ x_2(\xi_1, \xi_2) &= x_2^b(\xi_1) \left(\frac{\xi_2^t - \xi_2}{\xi_2^t - \xi_2^b}\right) \end{aligned}$$

for $-2\text{m} \le \xi_1 \le 3\text{m}$, $0 \le \xi_2 \le 1\text{m}$, $\xi_2^b = 0$, and $\xi_2^t = 1\text{m}$. The boundary conditions are the supersonic inflow on the left-hand side, the non-reflecting on the right-hand side, and the solid wall on the remaining sides. In Fig. 6, we show the Schlieren images and pseudo colors of pressure at six different times $t = 0.3$, 0.5, 0.7, 1.2, 1.6, and 2.5ms obtained using a 1000×200 grid. From the figure, it is easy to see that after the passage of the shock to the gas bubble, the upstream wall begins to spall across the bubble, yielding a refracted air shock traveling within it until its first reflection on the downstream bubble wall. Noticing that this upstream bubble wall would be involute eventually to form a jet which subsequently crosses the bubble and sends an intense blast wave out into the surrounding liquid. In the meantime, the incident shock wave along the bottom curved boundary would be diffracted into a simple Mach reflection.

To see the quantitative information of the solutions, Fig. 7 compares the cross section of the results along the $\xi_2 = 0.5\text{m}$ line with the same method but with a finer 2000×400 grid. Convergence of our computed solutions to the correct weak ones is clearly observed. In addition, Fig. 8 compares the cross section of the results for the same run along the bottom boundary with the results obtained using a Cartesian grid embedded boundary method [35]. The close agreement between the mapped grid and Cartesian grid results are seen also.

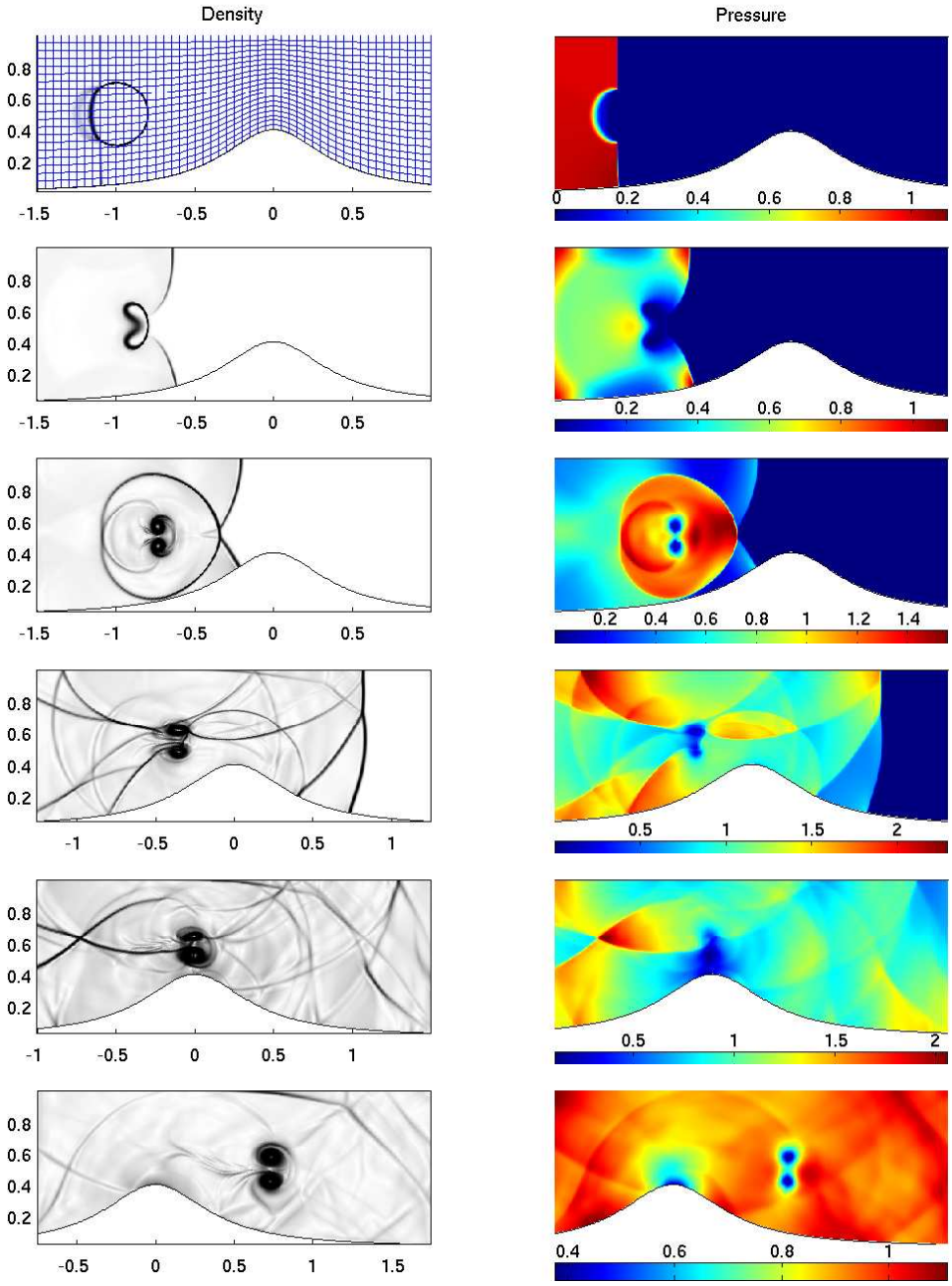

Figure 6: Numerical Schlieren images (on the left) and pseudo colors of pressure (on the right) for a planar shock wave in liquid over a circular gas bubble in a nozzle. Solutions from top to bottom are at times $t = 0.3$, 0.5, 0.7, 1.2, 1.6, and 2.5ms, and are plotted in a close neighborhood of the gas bubble. Here a sample of the quadrilateral grid is included in the first density plot to illustrate the basic physical grid system employed in the runs.

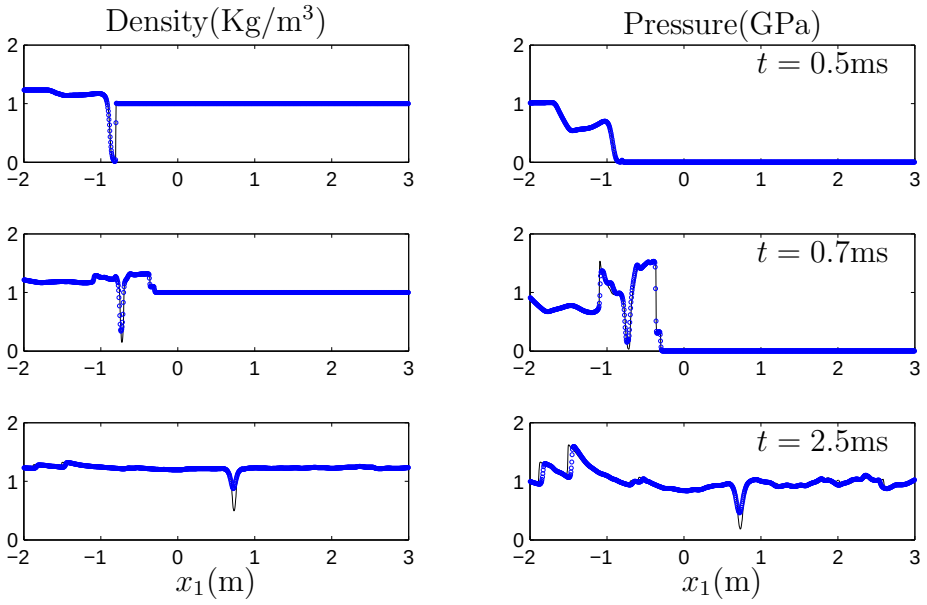

Figure 7: Cross-sectional plots of the results at the selected times $t = 0.5$, 0.7, and 2.5ms along the $\xi_2 = 0.5$m line, where the solid lines are results obtained using the same method but with a finer 2000×400 grid.

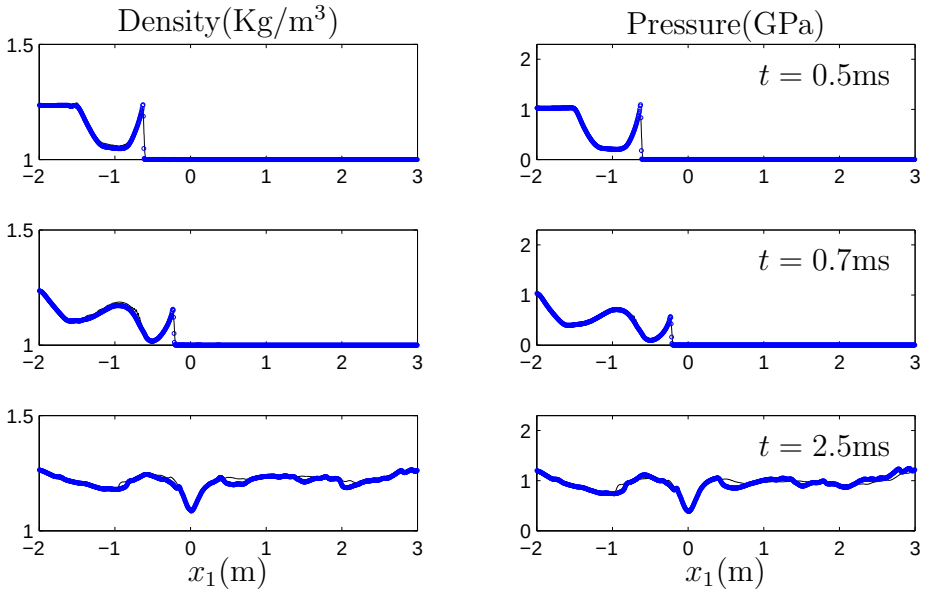

Figure 8: Cross-sectional plots of the results at the selected times $t = 0.5$, 0.7, and 2.5ms along the bottom boundary, where the solid lines are results obtained using using a Cartesian grid embedded boundary method [35] with the same grid size.

4.1.5. Underwater explosion with circular obstacles

Our next example for problems in more general geometries is an underwater explosion flow with circular obstacles, see [24] for a similar computation but with a square obstacle. In this test, the physical domain is a rectangular region of size $([-2,2]\times[-1.5,1])\text{m}^2$ in which inside the domain there are two circular obstacles, denoted by D_1 and D_2, with the centers $(\bar{x}_1^{D_1},\bar{x}_2^{D_1})=(-0.6,-0.8)\text{m}$ and $(\bar{x}_1^{D_2},\bar{x}_2^{D_2})=(0.6,-0.4)\text{m}$, respectively, and of the same radius $r_{D_1}=r_{D_2}=0.2\text{m}$. The initial condition we consider is composed of a horizontal air-water interface at $x_2=0$ and a circular gas bubble in water that lies below the interface. Here all the fluid components are at rest initially. When $x_2\geq 0$, the fluid is air with the state variables

$$(\rho,p)=\left(1.2\text{kg/m}^3,10^5\text{Pa}\right),$$

and when $x_2<0$ and $r<r_0$, the fluid is gas with the state variables

$$(\rho,p)=\left(1250\text{kg/m}^3,10^9\text{Pa}\right).$$

Now, in the remaining region where the obstacles do not belong to, the fluid is water with the states

$$(\rho,p)=\left(10^3\text{kg/m}^3,10^5\text{Pa}\right).$$

As before, the radial distance r is defined by $\sqrt{(x_1-\bar{x}_1)^2+(x_2-\bar{x}_2)^2}$, and we have $r_0=0.12\text{m}$ and $(\bar{x}_1,\bar{x}_2)=(0,-0.9)\text{m}$ in the current case. The material-dependent quantities for the gas- and liquid-phase are the same as in the previous tests.

We solve this problem using a mapped quadrilateral grid that is of the type described in [9]. In the current implementation of the algorithm, we have chosen the boundary data in regions inside the circular obstacles well so that there is no difficulty to solve the problem in the whole domain; this is a popular way to deal with inclusion problems numerically.

Figure 9 gives the numerical results of the density and pressure at six different times $t=0.24$, 0.4, 0.8, 1.2, 2.0, and 3.0ms, obtained using a 800×500 grid with the non-reflecting boundary on the top, and the solid wall boundary on the remaining sides. From the figure, it is easy to observe that in the early stage of the computation the flow field is essentially radial symmetry. Soon after the outward-going shock wave is reaching at the left obstacle and then the right obstacle, a reflected shock wave results from each

of the shock-obstacle collisions. As time goes on, these reflected shock waves would affect the structure of the gas bubble, and that induces numerous other wave-wave and wave-obstacle interactions at the later time. We note that when the outward-going shock is approaching at the air-water interface, we have a typical heavy-to-light shock-contact interaction, and the resulting wave pattern after the interaction would consist of a transmitted shock wave, an accelerated air-water interface, and a reflected rarefaction wave.

For practical applications, it is important to know how the effect of the impinging waves on the obstacles. As a measure of that, at each time t, we compute the surface pressure force exerted on the boundary of the obstacle by integrating the following line integral numerically:

$$F_i(t) = -\oint_{\partial D_i} p(t)\, ds$$

for the obstacle D_i, $i = 1, 2$. Figure 10 displays the results for that until the time $t = 3$ms, where a grid sequence, $2^i \times (200, 125)$ for $i = 0, 1, 2$, is used in the test to show the convergence behavior of the solution. From these graphs, the existence of positive pressure force is clearly seen in some time intervals, which mean the negative value of the pressure around the obstacles. This is, however, permitted in the current model with the stiffened gas equation as long as the pressure stays within the region of the thermodynamic stability. In a future work, we plan to include cavitation effect in the the problem formulation so as to have a more realistic model for the simulation (cf. [23, 24, 28, 41]).

4.2. Three-dimensional case

4.2.1. Smooth radially-symmetric flow

Our first test problem in three dimensions concerns an accuracy study of a smooth radially-symmetric flow (cf. [19]). In this problem, we assume a single-phase ideal gas flow with $\gamma = 1.4$ and $\mathcal{B} = 0$ in the equation of state, and take the flow condition that is at rest initially with the density $\rho(r) = 1+\exp(-30(r-1)^2)/10$ and pressure $p(r) = \rho^\gamma$ in a three-dimensional domain, where $r = \sqrt{x_1^2 + x_2^2 + x_3^2}$. For this problem, the solution will remain smooth and be spherical symmetry at least for the time interval considered.

We compare the behavior of the high-resolution wave propagation method on three different types of grids as depicted in Fig. 11:

Grid 1: Cartesian grids with cubical grid cells,

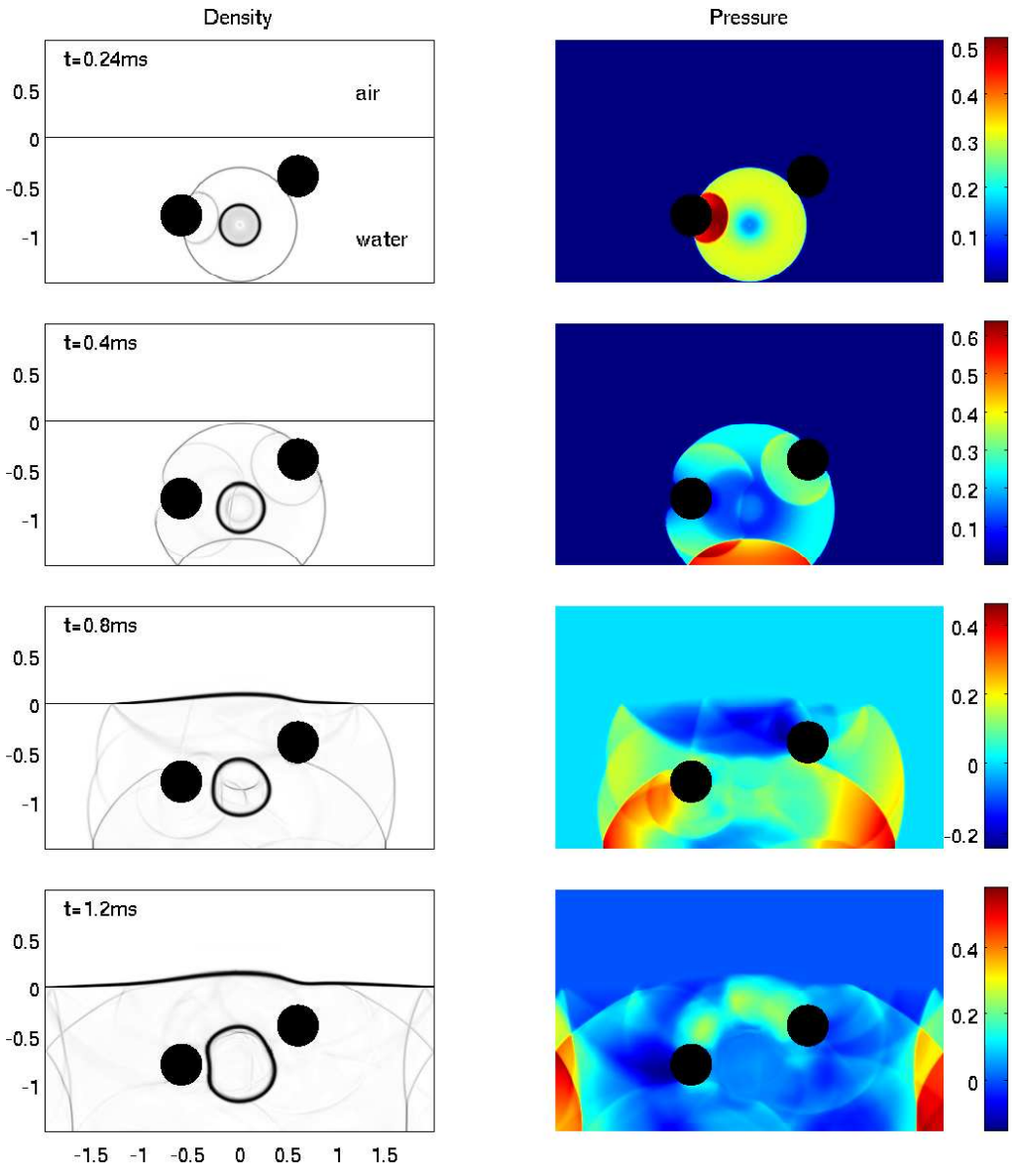

Figure 9: Numerical Schlieren images (on the left) and pseudo colors of pressure (on the right) for an underwater explosion problem with two circular obstacles. Solutions are shown at six different times $t = 0.24$, 0.4, 0.8, 1.2, 2.0, and 3.0ms, where a 800×500 grid was used in the computation.

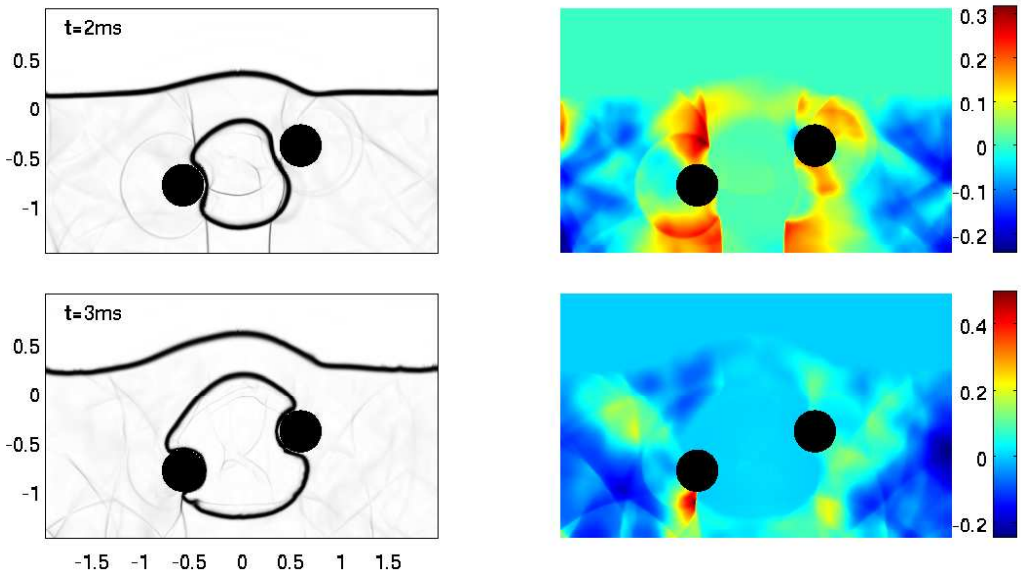

Figure 9: Continued.

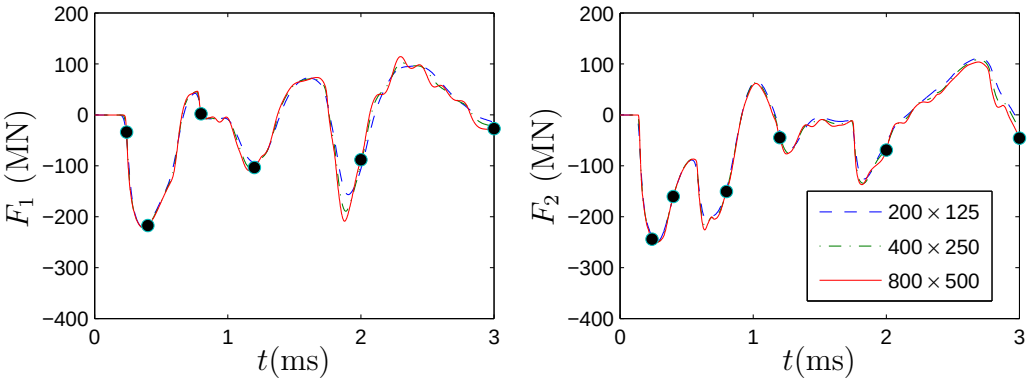

Figure 10: Convergence study of the time history of the pressure force on the circular obstacles for the underwater explosion problem. The filled circles in the graph are the results at the selected times shown in Fig. 9.

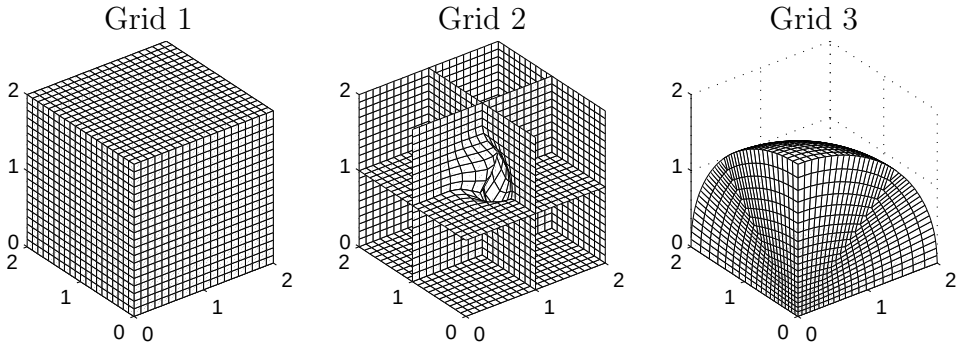

Figure 11: Three types of grids used for the smooth radially-symmetric flow problem.

Grid 2: Hexahedral grids of the type described in [10],

Grid 3: Hexahedral grids of the type in ball of radius 2 described in [9].

To estimate the order of accuracy of the method, for each grid type, we compute the solution at the mesh refinement sequence: $\Delta\xi_1^{(i)} = \Delta\xi_2^{(i)} = \Delta\xi_3^{(i)} = \Delta\xi^{(i)} = 2^{-i}/10$ for $i = 0, 1, 2, 3$, *i.e.*, by using an $N \times N \times N$ grid for $N = 20$, 40, 80 and 160. In each case, we carry out the computations using the Courant number $\nu = 0.7$, the Roe approximate Riemann solver, and no limiting. The symmetric boundary conditions are used at the boundaries $x_1 = 0$, $x_2 = 0$, and $x_3 = 0$, and the non-reflecting boundary conditions are used on the remaining edges (cf. [21]).

Numerical results at time $t = 0.3$ obtained from all the 12 tests are presented in Tables 4-6. Here the 1-norm and maximum-norm errors $\mathcal{E}_1(z)$ and $\mathcal{E}_m(z)$, for $z = \rho$, $|\vec{u}| = \sqrt{\sum_{i=1}^{3} u_i^2}$, and p are computed in each grid cell using the one-dimensional spherically-symmetric solution as the "true" solution. From the figures in these tables, the method is roughly second order accurate in most cases on this problem. The only exception is the behavior of the maximum-norm error of the total velocity $|\vec{u}|$, $\mathcal{E}_m(|\vec{u}|)$, on Grid 3 (this is a less smooth grid as compared to the other twos), where the convergence rate is anomalous.

4.2.2. Shock wave over dispersed phases in a cylindrical nozzle

Our final numerical example is on the simulation of a shock wave in liquid over dispersed (gas and solid) phases in a cylindrical nozzle. In this test, the physical domain is a cylindrical region that is form by rotating the bounded

Table 4: High-resolution results for the smooth radially-symmetric test on Grid 1; 1- and maximum-norm errors in primitive variables are shown.

N	$\mathcal{E}_1(\rho)$	Order	$\mathcal{E}_1(\lvert\vec{u}\rvert)$	Order	$\mathcal{E}_1(p)$	Order
20	$7.227 \cdot 10^{-3}$		$8.920 \cdot 10^{-3}$		$1.019 \cdot 10^{-2}$	
40	$2.418 \cdot 10^{-3}$	1.58	$2.558 \cdot 10^{-3}$	1.80	$3.415 \cdot 10^{-3}$	1.58
80	$6.356 \cdot 10^{-4}$	1.93	$6.754 \cdot 10^{-4}$	1.92	$8.980 \cdot 10^{-4}$	1.93
160	$1.616 \cdot 10^{-4}$	1.98	$1.718 \cdot 10^{-4}$	1.97	$2.282 \cdot 10^{-4}$	1.98

N	$\mathcal{E}_m(\rho)$	Order	$\mathcal{E}_m(\lvert\vec{u}\rvert)$	Order	$\mathcal{E}_m(p)$	Order
20	$1.096 \cdot 10^{-2}$		$1.200 \cdot 10^{-2}$		$1.569 \cdot 10^{-2}$	
40	$4.085 \cdot 10^{-3}$	1.42	$4.381 \cdot 10^{-3}$	1.45	$5.848 \cdot 10^{-3}$	1.42
80	$1.235 \cdot 10^{-3}$	1.73	$1.263 \cdot 10^{-3}$	1.79	$1.765 \cdot 10^{-3}$	1.73
160	$3.517 \cdot 10^{-4}$	1.81	$3.349 \cdot 10^{-4}$	1.91	$5.030 \cdot 10^{-4}$	1.81

Table 5: High-resolution results for the smooth radially-symmetric test on Grid 2; 1- and maximum-norm errors in primitive variables are shown.

N	$\mathcal{E}_1(\rho)$	Order	$\mathcal{E}_1(\lvert\vec{u}\rvert)$	Order	$\mathcal{E}_1(p)$	Order
20	$7.227 \cdot 10^{-3}$		$8.920 \cdot 10^{-3}$		$1.019 \cdot 10^{-2}$	
40	$2.418 \cdot 10^{-3}$	1.58	$2.558 \cdot 10^{-3}$	1.80	$3.415 \cdot 10^{-3}$	1.58
80	$6.356 \cdot 10^{-4}$	1.93	$6.754 \cdot 10^{-4}$	1.92	$8.980 \cdot 10^{-4}$	1.93
160	$1.616 \cdot 10^{-4}$	1.98	$1.718 \cdot 10^{-4}$	1.97	$2.282 \cdot 10^{-4}$	1.98

N	$\mathcal{E}_m(\rho)$	Order	$\mathcal{E}_m(\lvert\vec{u}\rvert)$	Order	$\mathcal{E}_m(p)$	Order
20	$7.227 \cdot 10^{-3}$		$8.920 \cdot 10^{-3}$		$1.019 \cdot 10^{-2}$	
40	$2.418 \cdot 10^{-3}$	1.58	$2.558 \cdot 10^{-3}$	1.80	$3.415 \cdot 10^{-3}$	1.58
80	$6.356 \cdot 10^{-4}$	1.93	$6.754 \cdot 10^{-4}$	1.92	$8.980 \cdot 10^{-4}$	1.93
160	$1.616 \cdot 10^{-4}$	1.98	$1.718 \cdot 10^{-4}$	1.97	$2.282 \cdot 10^{-4}$	1.98

Table 6: High-resolution results for the smooth radially-symmetric test on Grid 3; 1- and maximum-norm errors in primitive variables are shown.

N	$\mathcal{E}_1(\rho)$	Order	$\mathcal{E}_1(\lvert\vec{u}\rvert)$	Order	$\mathcal{E}_1(p)$	Order
20	$1.290 \cdot 10^{-2}$		$1.641 \cdot 10^{-2}$		$1.816 \cdot 10^{-2}$	
40	$4.694 \cdot 10^{-3}$	1.46	$4.999 \cdot 10^{-3}$	1.71	$6.623 \cdot 10^{-3}$	1.46
80	$1.257 \cdot 10^{-3}$	1.90	$1.379 \cdot 10^{-3}$	1.86	$1.774 \cdot 10^{-3}$	1.90
160	$3.209 \cdot 10^{-4}$	1.97	$3.546 \cdot 10^{-4}$	1.96	$4.527 \cdot 10^{-4}$	1.97

N	$\mathcal{E}_m(\rho)$	Order	$\mathcal{E}_m(\lvert\vec{u}\rvert)$	Order	$\mathcal{E}_m(p)$	Order
20	$1.632 \cdot 10^{-2}$		$1.984 \cdot 10^{-2}$		$2.316 \cdot 10^{-2}$	
40	$5.819 \cdot 10^{-3}$	1.49	$6.745 \cdot 10^{-3}$	1.56	$8.307 \cdot 10^{-3}$	1.48
80	$1.823 \cdot 10^{-3}$	1.67	$4.290 \cdot 10^{-3}$	0.65	$2.710 \cdot 10^{-3}$	1.67
160	$5.053 \cdot 10^{-4}$	1.85	$3.271 \cdot 10^{-3}$	0.39	$7.237 \cdot 10^{-4}$	1.85

region:

$$z\left(x_1\right) = \frac{1}{2}\left(x_1 - \frac{3}{2}\right)^2 + \frac{3}{5}, \quad x_1 \in [0,3]\text{m},$$

about the x_1-axis. For this problem, the initial condition consists of a planar rightward-going shock wave in water at $x_1 = 0.2$m and a set of $M_d \geq 1$ stationary spherical dispersed phases that lies on the right of the shock wave. For convenience, we use D_i to denote the ith dispersed phase for $i = 1, 2, \ldots, M_d$.

For both the shock wave and the material quantities in the background fluid, the water, we take the same set of data as employed in Section 4.1.4. For the dispersed phase D_1, inside the sphere with the center $(\bar{x}_1^{D_1}, \bar{x}_2^{D_1}, \bar{x}_3^{D_1}) = (0.5, 0, 0)$m and radius $r_{D_1} = 0.2$m, the material is gas with the state variables

$$(\rho, p, \gamma, \rho_0, \mathcal{B}) = \left(50\text{kg/m}^3, 10^5\text{Pa}, 1.4, 50\text{kg/m}^3, 0\right).$$

For the dispersed phases D_2, D_3, D_4, and D_5, however, inside the spheres with the center $(\bar{x}_1^{D_2}, \bar{x}_2^{D_2}, \bar{x}_3^{D_2}) = (1.2, 0, 0.3)$m, $(\bar{x}_1^{D_3}, \bar{x}_2^{D_3}, \bar{x}_3^{D_3}) = (1.8, -0.2, 0)$m, $(\bar{x}_1^{D_2}, \bar{x}_2^{D_2}, \bar{x}_3^{D_2}) = (1.2, 0, -0.3)$m, $(\bar{x}_1^{D_3}, \bar{x}_2^{D_3}, \bar{x}_3^{D_3}) = (1.8, 0.2, 0)$m, and radius $r_{D_i} = 0.12$m for $i = 1, 2, 3, 4$, the material is aluminum with the data

$$(\rho, p, \gamma, \rho_0, \mathcal{B}) = \left(2785\text{kg/m}^3, 10^5\text{Pa}, 3, 2785\text{kg/m}^3, 2.84 \times 10^7(\text{m/s})^2\right).$$

Note that this gives us an example that involves three phases (water, gas, and solid) in the problem formulation. Due to the symmetry in both the

geometry and the initial condition, we only take a quarter of the nozzle where $x_1 \in [0, 3]$m, $x_2 \leq 0$ and $x_3 \geq 0$, in carrying out the runs. Boundary conditions we used are supersonic inflow on the left, non-reflecting on the right faces, and solid wall on the remaining top, bottom, front, and back faces.

To discretize this cylindrical nozzle, since the cross-section of the nozzle in the plane perpendicular to the x_1-axis at x_1 is a circular disk of radius $z(x_1)$, it is easy to use a hexahedral grid of the type described in [9] for the computations. Numerical results of a sample run using a $300 \times 100 \times 100$ grid are shown in Fig. 12. Here volumetric slice planes and contour lines at $x_2 = 0$ and $x_3 = 0$ are plotted for the density and pressure at times $t = 0.1$, 0.3, 0.4, 0.6, 0.8, and 1.0ms. The passage of the incident shock wave to the dispersed phases results in clearly the collapse of the gas bubble and the deformation of solid aluminum at a later time, which are common phenomena observed in shock wave problems with dispersed phases (cf. [33, 34]). As to the computed pressure near the water-gas and water-solid interfaces, we again see smooth transition of the solutions without any spurious oscillations.

To demonstrate the convergence behavior of the solution, we solve the problem using the mesh refinement sequence: $75 \times 25 \times 25$, $150 \times 50 \times 50$, and $300 \times 100 \times 100$, and measure the temporal resolution of the circulation, denoted by Γ_i, along the boundary curve of the $x_i = 0$ plane. Figure 13 shows the results for the $i = 2$ and 3 case, observing good agreement of the solution behavior as the mesh is refined.

5. Conclusion

We have presented a simple mapped-grid approach for the numerical resolution of compressible multiphase problems with a stiffened gas equation of state in general two- and three-dimensional geometries. The algorithm uses a curvilinear coordinates formulation of mathematical models that is devised to ensure a consistent approximation of the mass and energy equations near the numerical-induced smeared material interfaces, and also a direct computation of the pressure from the equation of state. A standard high-resolution wave propagation method is employed to solve the proposed multiphase models that shows second order accurate results for smooth flow problems and also free of spurious oscillations in the pressure for problems with interfaces. Ongoing works are to extend this approach further to moving mesh methods, and to multiphase problems with cavitations and phase transitions.

Acknowledgement

This work was supported in part by National Science Council of Taiwan Grant 96-2115-M-002-008-MY3.

References

[1] R. Abgrall. How to prevent pressure oscillations in multicomponent flow calculations: a quasi conservative approach. *J. Comput. Phys.*, 125:150–160, 1996.

[2] R. Abgrall, B. Nkonga, and R. Saurel. Efficient numerical approximations of compressible multi-material flow for unstructured meshes. *Computers and Fluids*, 32(4):571–605, 2003.

[3] G. Allaire, S. Clerc, and S. Kokh. A five-equation model for the simulation of interface between compressible fluids. *J. Comput. Phys.*, 181:577–616, 2002.

[4] D. A. Anderson, J. C. Tannehill, and R. H. Pletcher. *Computational Fluid Mechanics and Heat Transfer*. McGraw-Hill, New York, 1984.

[5] J. W. Banks, D. W. Schwendeman, A. K. Kapila, and W. D. Henshaw. A high-resolution Godunov method for compressible multi-material flow on overlapping grids. *J. Comput. Phys.*, 223:262–297, 2007.

[6] J. U. Brackbill, D. B. Kothe, and C. Zemach. A continuum method for modeling surface tension. *J. Comput. Phys.*, 100:335–354, 1992.

[7] D. L. Brown. An unsplit Godunov method for systems of conservation laws on curvilinear overlapping grids. *Math. Comput. Modelling*, 20:29–48, 1994.

[8] D. A. Calhoun, C. Helzel, and R. J. LeVeque. A finite volume grid for solving hyperbolic problems on the sphere. In *Hyperbolic Problems: Theory, Numerics, Applications*, pages 355–362. Springer-Verlag, 2008.

[9] D. A. Calhoun, C. Helzel, and R. J. LeVeque. Logically rectangular grids and finite volume methods for PDEs in circular and spherical domains. *SIAM Review*, 50(4):723–752, 2008. Webpage to accompany this paper: http://www.amath.washington.edu/∼rjl/pubs/circles/index.html.

[10] D. A. Calhoun and R. J. LeVeque. An accuracy study of mesh refinement on mapped grids. In *Adaptive mesh refinement, theory, and applications: proceedings of the Chicago Workshop on Adaptive Mesh Refinement Methods, Sept. 3-5, 2003*, Lecture note in computational science and engineering, pages 91–102. Springer, New York, 2005.

[11] G. Chen, H. Tang, and P. Zhang. Second-order accurate Godunov scheme for multicomponent flows on moving triangular meshes. *J. Sci. Comput.*, 34:64–86, 2008.

[12] J. Cheng and C.-W. Shu. A high order ENO conservative Lagrangian type scheme for the compressible Euler equations. *J. Comput. Phys.*, 227:1567–1596, 2007.

[13] R. Courant and K. O. Friedrichs. *Supersonic Flow and Shock waves*. Wiley-Interscience, New York, 1948.

[14] F. Harlow and A. A. Amsden. *Fluid Dynamics*. Los Alamos National Laboratory, Los Alamos, NM, 1971. Monograph LA-4700.

[15] W. D. Henshaw and D. W. Schwendeman. Moving overlapping grids with adaptive mesh refinement for high-speed reactive and non-reactive flow. *J. Comput. Phys.*, 216:744–779, 2006.

[16] K. A. Hoffmann and S. T. Chiang. *Computational Fluid Dynamics*. Engineering Education System, Wichita, Kansas, USA, 4 edition, 2000.

[17] W. Jang, J. Jilesen, F. S. Lien, and H. Ji. A study on the extension of a VOF/PLIC based method to curvilinear coordinate system. *Int. J. Comput. Fluid Dyn.*, 22(4):241–257, 2008.

[18] A. K. Kapila, R. Menikoff, J. B. Bdzil, S. F. Son, and D. S. Stewart. Two-phase modeling of deflagration-to-denonation transition in granular materials: reduced equations. *Phys. Fluids*, 13(10):3002–3024, 2001.

[19] J. O. Langseth and R. J. LeVeque. A wave propagation method for three-dimensional hyperbolic conservation laws. *J. Comput. Phys.*, 165:126–166, 2000.

[20] R. J. LeVeque. High resolution finite volume methods on arbitrary grids via wave propagation. *J. Comput. Phys.*, 78:36–63, 1988.

[21] R. J. LeVeque. *Finite Volume Methods for Hyperbolic Problems*. Cambridge University Press, 2002.

[22] R. J. LeVeque. Python tools for reproducible research on hyperbolic problems. *Computing in Science and Engineering*, 11:19–27, 2009.

[23] T. G. Liu, B. C. Khoo, and W. F. Xie. Isentropic one-fluid modelling of unsteady cavitating flow. *J. Comput. Phys.*, 201:80–108, 2004.

[24] T. G. Liu, B. C. Khoo, K. S. Yeo, and C. Wang. Underwater shock-free surface-structure interaction. *Int. J. Numer. Meth. Engng*, 58:609–630, 2003.

[25] R. Menikoff and B. Plohr. The Riemann problem for fluid flow of real materials. *Rev. Mod. Phys.*, 61:75–130, 1989.

[26] G. Perigaud and R. Saurel. A compressible flow model with capillary effects. *J. Comput. Phys.*, 209:139–178, 2005.

[27] F. Petitpas, J. Massoni, R. Saurel, E. Lapebie, and L. Munier. Diffuse interface model for high speed cavitating underwater systems. *Int. J. Multiphase Flow*, 35:747–759, 2009.

[28] R. Saurel, F. Petitpas, and R. A. Berry. Simple and efficient relaxation methods for interfaces separating compressible fluids, cavitating flows and shocks in multiphase mixtures. *J. Comput. Phys.*, 228:1678–1712, 2009.

[29] C.-W. Shu. Essentially non-oscillatory and weighted essentially non-oscillatory schemes for hyperbolic conservation laws. In B. Cockburn, C. Johnson, C.-W. Shu, and E. Tadmor, editors, *Advanced Numerical Approximation of Nonlinear Hyperbolic Equations*, pages 325–432. Springer, Berlin, 1998. Lecture Notes in Mathematics, vol. 1697.

[30] K.-M. Shyue. An efficient shock-capturing algorithm for compressible multicomponent problems. *J. Comput. Phys.*, 142:208–242, 1998.

[31] K.-M. Shyue. A fluid-mixture type algorithm for compressible multicomponent flow with van der Waals equation of state. *J. Comput. Phys.*, 156:43–88, 1999.

[32] K.-M. Shyue. A fluid-mixture type algorithm for compressible multicomponent flow with Mie-Grueneisen equation of state. *J. Comput. Phys.*, 171:678–707, 2001.

[33] K.-M. Shyue. A fluid-mixture type algorithm for barotropic two-fluid flow problems. *J. Comput. Phys.*, 200:718–748, 2004.

[34] K.-M. Shyue. A volume-fraction based algorithm for hybrid barotropic and non-barotropic two-fluid flow problems. *Shock Waves*, 15(6):407–423, 2006.

[35] K.-M. Shyue. A moving-boundary tracking algorithm for inviscid compressible flow. In *Hyperbolic Problems: Theory, Numerics, Applications*, pages 989–996. Springer-Verlag, 2008.

[36] K.-M. Shyue. A high-resolution mapped grid algorithm for compressible multiphase flow problems, webpage to accompany this paper, 2010. http://www.math.ntu.edu.tw/∼shyue/preprints/mphase-mappedgrid.html.

[37] K.-M. Shyue. *Front Tracking Methods based on Wave Propagation*. PhD thesis, University of Washington, June, 1993. Available at the URL http://www.math.ntu.edu.tw/∼shyue/preprints/thesis.pdf.

[38] H. Tang and T. Tang. Adaptive mesh methods for one- and two-dimensional hyperbolic conservation laws. *SIAM J. Numer. Anal.*, 41:487–515, 2003.

[39] J. F. Thompson, B. K. Soni, and N. P. Weatherill. *Handbook of Grid Generation*. CRC Press, 1999.

[40] A. van Dam and P. A. Zegeling. Balanced monitoring of flow phenomena in moving mesh methods. *Comm. Comput. Phys.*, 7:138–170, 2010.

[41] A. B. Wardlaw, Jr. and J. A. Luton. Fluid-structure mechanisms for close-in explosions. *Shock and Vibration*, 7:265–275, 2000.

[42] P. Wesseling. *Principles of Computational Fluid Dynamics*. Springer-Verlag, 2001.

[43] H. W. Zheng, C. Shu, and Y. T. Chew. An objected-oriented quadrilateral-mesh based solution adaptive algorithm for compressible multifluid flows. *J. Comput. Phys.*, 227:6895–6921, 2008.

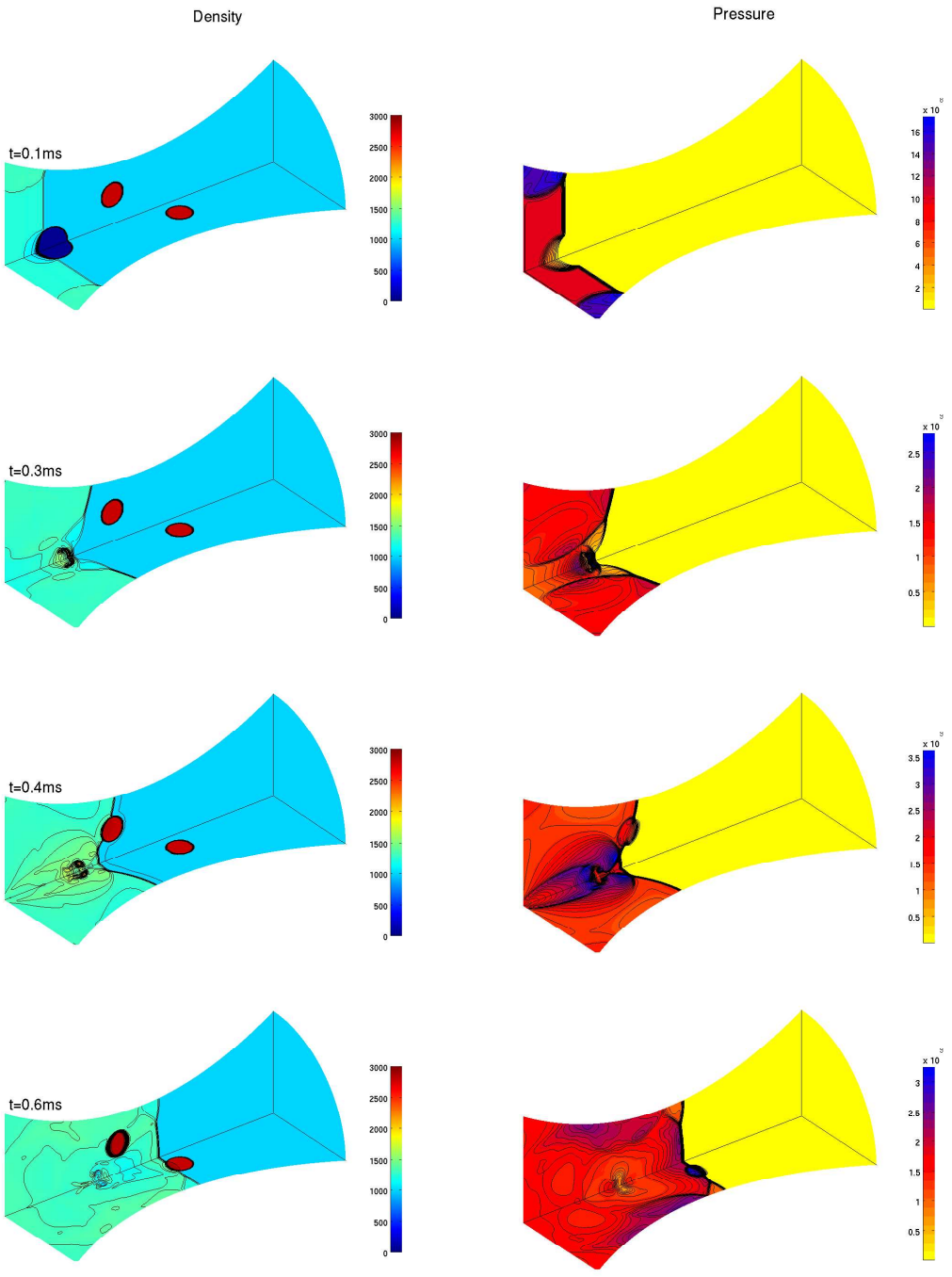

Figure 12: Numerical results for the simulation of a shock wave in water over dispersed (gas and solid) phases in a cylindrical nozzle. Solutions from the top to bottom are at times $t = 0.1$, 0.3, 0.4, 0.6, 0.8, and 1.0ms, where volumetric slice planes and contour lines are plotted for the density and pressure at $x_2 = 0$ and $x_3 = 0$.

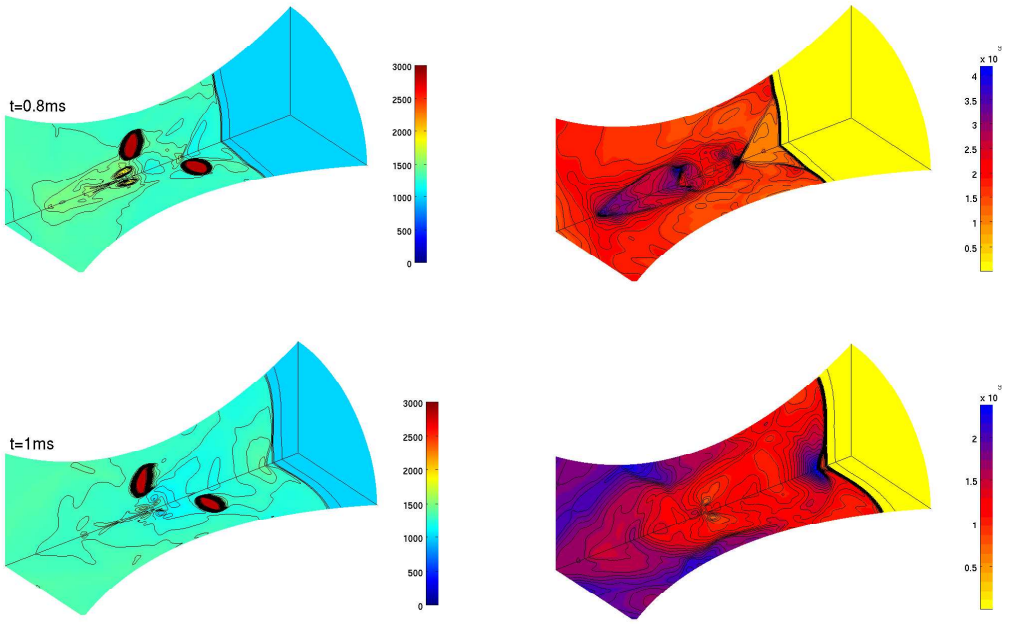

Figure 12: Continued.

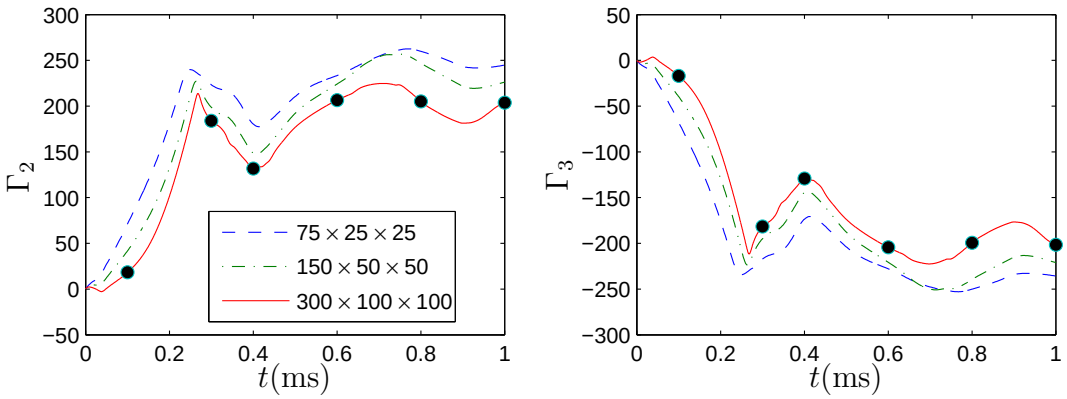

Figure 13: A convergence study of the circulation for a shock wave over spherical dispersed phases in a cylindrical nozzle. Temporal solutions are shown along the boundary curves of the $x_2 = 0$ (on the left) and $x_3 = 0.0$ (on the right) planes using three different mesh sizes. The filled circles in the graph are the results at the selected times shown in Fig. 12.